TAMPERE UNIVERSITY OF TECHNOLOGY

RIKU RAATIKAINEN

# MODELLING OF THE THERMO-MECHANICAL BEHAVIOR OF THE TWO-BEAM MODULE FOR THE COMPACT LINEAR COLLIDER

Master of Science Thesis

Examiners: Professor Arto Lehtovaara,
D.Sc. Sami Pajunen
Examiners and topic approved in the Department of Mechanics and Design Council meeting on 7.9.2011

# ABSTRACT

TAMPERE UNIVERSITY OF TECHNOLOGY
Master's Degree Programme in Mechanical Engineering
**RIKU RAATIKAINEN : MODELLING OF THE THERMO-MECHANICAL BEHAVIOR OF THE TWO-BEAM MODULE FOR THE COMPACT LINEAR COLLIDER**
Master of Science Thesis, 59 pages, 14 appendix pages
December 2011
Major: Applied Mechanics
Examiners: Professor Arto Lehtovaara, D.Sc. Sami Pajunen
Supervisors: Ph.D. Kenneth Österberg, Dr. Germana Riddone
Keywords: Thermo-Mechanical Modelling, Linear Particle Collider, CLIC, Finite Element Method, FEM, Fluid Dynamics, Heat Transfer, CFD

To fulfil the mechanical requirements set by the luminosity goals of the compact linear collider, the 2-m long two-beam modules, the shortest repetitive elements in the main linear accelerator, have to be controlled at micrometer level. At the same time these modules are exposed to high power dissipation that varies while the accelerator is ramped up to nominal power and when the mode of the accelerator operation is modified. These variations will give rise to inevitable temperature transients driving mechanical distortions in and between different module components. Therefore, the thermo-mechanical behaviour of the module is of a high importance.

This thesis describes a finite element method model for the two-beam compact linear collider module. The components are described in detail compared to earlier models, which should result in a realistic description of the module. Due to the complexity of the modules, the modelling is divided into several phases from geometrical simplification and modification to the creation of appropriate cooling environment and finally towards full-scale thermo-mechanical behavior of the accelerator in its primary operation modes.

The thermal and structural results for the new module configuration are presented and the thermo-mechanical behavior of the module in its primary operation modes is discussed. These results will be compared with the forthcoming laboratory measurements. Improved understanding of the module's thermo-mechanical behavior and its simulation model can then be propagated to the following module generations using the model presented in this thesis as a baseline.

# TIIVISTELMÄ

TAMPEREEN TEKNILLINEN YLIOPISTO
Konetekniikan koulutusohjelma
**RIKU RAATIKAINEN : LINEAARISEN HIUKKASKIIHDYTINMODUULIN TERMOMEKAANINEN MALLINTAMINEN**
Diplomityö, 59 sivua, 14 liitettä
Joulukuu 2011
Pääaine: Teknillinen mekaniikka
Tarkastajat: Professori Arto Lehtovaara, TkT Sami Pajunen
Ohjaajat: TkT Germana Riddone, FT Kenneth Österberg
Avainsanat: Termomekaaninen mallintaminen, lineaarikiihdytin, CLIC, elementtimenetelmä, FEM, virtausdynamiikka, lämmönsiirto, CFD

Tulevaisuuden sekä mahdollisen seuraavan sukupolven lineaarisen hiukkaskiihdytinprojektin päämääränä on osoittaa noin 2-metrisistä kiihdytinmoduuleista koostuvan sekä yhteensä noin 48.3 km pituisen normaalikonduktiivisen törmäyttimen mahdollistava teknologia. Haastavien tarkkuusvaatimusten vuoksi, CLIC-moduulit täytyy voida stabiloida mikrometriasteella. Samaan aikaan moduulit altistuvat erilaisille kuormituksille kuten gravitaatiolle, paine-erosta aiheutuville tyhjiövoimille sekä muuttuville lämpökuormille, jotka yhdessa aiheuttavat niihin merkittävät lämpötilamuutokset sekä mekaaniset muodonmuutokset. Täten moduulien kytketty termomekaaninen käyttäytyminen nousee suunnittelussa erittäin merkittävään rooliin. Tässä diplomityössä kuvataan elementtimenetelmään perustuva lineaarisen kiihdytinmoduulin termomekaanista käyttäytymistä kuvaava simulaatiomalli. Mallin komponentit perustuvat jo suunniteltuihin ja tulevaisuudessa testattaviin osiin. Sillä moduulit ovat itsessään hyvin kompleksisia, mallintaminen jaettiin useisiin pienempiin osiin lähtien mallin yksinkertaistamisesta ja muokkaamisesta jäähdytysverkon luomiseen sekä edelleen kohti moduulin termomekaanista mallintamista.

Työstä saadut tulokset näyttävät moduulin lämpötila ja siirtymäkentät kiihdyttimen toimiessa nimellisalueellaan. Tulosten mukaan nykyinen jäähdytysjärjestelmä nostaa moduulin keskimääräistä lämpötilaa useilla asteilla sekä yhdessä muiden kuormitusten kanssa aiheuttaa siihen useiden kymmenien mikrometrien siirtymiä. Erot moduulin rakenteiden siirtymissä kiihdyttimen eri toimintavaiheissa ovat vaadittujen tarkkuuksien sisällä. Työstä saatuja tuloksia tullaan vertaamaan jatkossa suunniteltuihin laboratoriomittauksiin, joiden avulla nykyistä mallia pystytään yhä parantamaan. Työn johtopäätösosiossa otetaan myös kantaa mahdollisiin kehitysnäkökulmiin itse suunnittelussa, joita parantamalla moduulin termomekaanista käyttäytymistä voitaisiin parantaa edelleen nykyisestä.

# ACKNOWLEDGEMENT

The research leading to this thesis has got funding from the European Coordination for Accelerator Research and Development (EuCARD) project, which is a common venture of 37 European Accelerator Laboratories, Institutes, Universities and Industrial Partners involved in accelerator sciences and technologies. The thesis was carried out in CERN in a close collaboration with Helsinki Institute of Physics (HIP). Therefore, I would like to first grant thankfulness to these participants providing me an opportunity to realise this research work. Furthermore, I would like to thank my supervisors Dr. Germana Riddone and Ph.D. Kenneth Österberg for their guidance and support during the development of the CLIC Two-Beam module simulation model. I also thank my examiners Prof. Arto Lehtovaara and D.Tech. Sami Pajunen for their technical suggestions and for looking over the thesis. Finally, I would like to lay a great appreciation to the people in the CLIC Working group in CERN whose collaboration was largely respected.

Geneva, November 15, 2011

Riku Raatikainen

# CONTENTS

# NOTATIONS

| | | |
|---|---|---|
| $f_{RF}$ | accelerator frequency | [Hz] |
| L | luminosity | $[\frac{1}{cm^2 s}]$ |
| $\mu$ | viscosity | $[\frac{kg}{sm}]$ |
| $\rho$ | density | $[\frac{kg}{m^3}]$ |
| $x, y, z$ | cartesian coordinate directions | |
| $u, v, w$ | velocity components | $[\frac{m}{s}]$ |
| p | pressure | $[Pa]$ |
| $C_s$ | specific heat | $[\frac{J}{kgK}]$ |
| $\dot{m}$ | mass flow rate | $[\frac{kg}{s}]$ |
| $\Delta T$ | temperature difference | $[K]$ |
| $\dot{Q}$ | heat dissipation | $[W]$ |
| $a$ | iris radius | [m] |
| $\lambda$ | wavelength | [m] |
| $d$ | iris thickness | [m] |
| $v_g$ | group velocity | $[\frac{m}{s}]$ |
| $N_c$ | number of cells | |
| $N_s$ | bunch separation | |
| $N$ | bunch population | |
| $N_b$ | number of bunches in a train | |
| $t_f$ | filling time | [s] |
| $t_r$ | rise time | [s] |
| $t_p$ | pulse length | [s] |
| $P_{in}$ | input power | [W] |
| $E_{surf}$ | surface field | $[\frac{V}{m}]$ |
| $T_{max}$ | maximum temperature rise | $[K]$ |
| $\eta$ | efficiency | [%] |
| $N_{unit}$ | no. of drive beam sectors | |
| $L_{unit,total}$ | unit length (total) | [m] |
| $N_{PETS,unit}$ | no. PETS / sector | |
| $L_{PETS,unit}$ | length of PETS (active) | [m] |
| $P_{acc}$ | main beam acceleration power | [W] |
| $\Delta E_{main}$ | main beam energy gain | [eV] |
| $\eta_{decRF}$ | drive beam RF efficiency | [%] |
| $E_{in,dec}$ | energy (decelerator injection) | [eV] |
| $E_{fin,dec}$ | energy (final, minimum) | [eV] |
| $I_{dec}$ | average current in pulse | [A] |
| $\tau_{train}$ | train duration | [s] |

| | | |
|---|---|---|
| $N_{b.dec}$ | no. of bunches / train | |
| $f_{rep}$ | repetitive frequency | [Hz] |
| $N_c$ | no. of parallel flows | |
| $\mathbf{C^t}$ | specific heat matrix | |
| $\dot{\mathbf{T}}$ | transient thermal vector | |
| $\mathbf{K^t}$ | thermal conductivity matrix | |
| $\mathbf{K^p}$ | pressure conductivity matrix | |
| $\mathbf{T}$ | nodal temperature vector | |
| $\mathbf{P}$ | nodal pressure vector | |
| $\mathbf{T}$ | nodal pressure vector | |
| $\mathbf{Q}$ | nodal heat flow vector | |
| $\mathbf{W}$ | fluid flow vector | |
| $\mathbf{Q^g}$ | internal heat generation vector | |
| $\mathbf{H}$ | gravity and pumping effects vector | |
| $v_a$ | additional velocity | $[\frac{m}{s}]$ |
| $P_{PMP}$ | pump pressure | $[\frac{N}{m^2}]$ |
| $C_L$ | loss coefficient | |
| $\overline{u'^2}, \overline{v'^2}, \overline{w'^2}$ | average stress components | $[\frac{N}{m^2}]$ |

# ABBREVIATIONS

| | |
|---|---|
| APDL | Ansys Parametric Design Language |
| AS | Accelerating Structure |
| BPM | Beam Position Monitor |
| CDR | Conceptual Design Report |
| CERN | European Organization for Nuclear Research |
| CLIC | Compact Linear Collider |
| CFD | Computational Fluid Dynamics |
| CMF | Choke Mode Flange |
| DBQ | Drive Beam Quadrupole |
| DOF | Degree of Freedom |
| EDMS | Electronic Data Management System |
| FEM | Finite Element Method |
| ILC | International Linear Collider |
| LEP | Large Electron-Positron Collider |
| LHC | Large Hadron Collider |
| PETS | Power Extraction and Transfer Structure |
| RF | Radio Frequency |
| SAS | Super-Accelerating-Structure |
| TMM | Thermo Mechanical Model |

| | |
|---|---|
| WFM | Wave Field Monitor |
| WG | Waveguide |

# 1. INTRODUCTION

## 1.1 Background

Founded in 1954 by 12 countries in Western Europe the European Organization for Nuclear Research, known as CERN, is one of the world's largest and respected particle physics laboratory situated in the Franco-Swiss border near Geneva. The top priorities at CERN in the 21st century will be experiments probing beyond the Standard Model of particle physics. Today CERN is run by 20 Member States but many non-European countries are also involved in different ways to the research programs. [1, 2] Currently just under 2400 people are employed by CERN but over 10 000 visiting scientist are related to the ongoing projects through their research. They represent about 608 universities and 113 nationalities. [3] CERN's main function is to provide particle accelerators for the high-energy physics research. As an outcome, historically several important achievements have been made in physics and furthermore, the research work related to particle accelerator studies has revolutionized the technology used in many other fields such as biology, radiology and medicine. In the 1970's, for example, CERN had an important role in the discovery and emerging of the technology of positron emission tomography (PET), which enables three-dimensional imaging of functional processes in the brain. [4] More recently, CERN has become a centre for the development of the grid network, which nowadays enables the handling of the large amount of data produced by current accelerator projects.

Since the year 2008 CERN's foremost accelerator, the LHC (Large Hadron Collider), has been exploring the new terascale energy region. The LHC tunnel is located 100 meters underground and it uses a 27 km circumference circular tunnel previously occupied by LEP (Large Electron-Positron Collider) which was closed down in November 2000. In coming years the LHC is believed to confirm or refute the existence of the Higgs boson of the Standard Model and furthermore reveal the possibilities of physics beyond the Standard Model, such as supersymmetry, extra dimensions and new gauge bosons. However, it is impossible to expect that the experiments at the LHC will answer all the questions concerning new physics explored at TeV range. Many of the open questions can be addressed best by a lepton-antilepton (e.g. electron-positron) collider. Hence, the particle physicists worldwide have reached a consensus that the results from the LHC will need to be complemented by experiments at an electron-positron collider operating in the tera-electron-volt energy range. [5]

In a circular colliders the particles to be accelerated emit synchrotron radiation, causing significant energy losses, which has to be replaced by a powerful RF-acceleration system. In LEP the highest centre-of-mass energy in electron-positron collision was 209 GeV, where each beam particle loss around the the accelerator due to synchrotron radiation were about 3 % of its energy each turn. The biggest superconductive RF-system built so far was just enough to keep the beam at its nominal energy. Moreover the synchrotron radiation increases with the fourth power of the energy of the circulating beam. Thus, it is clear that for an electron-positron collider operating in energy region above LEP the amount of RF-power needed to keep the beam circulating becomes larger than can be provided. Therefore, the only feasible option for actualising electron-positron collider operating in the Multi-TeV energy range is a linear accelerating collider. As today, two approaches to linear colliders are being developed, International Linear Collider (ILC) and Compact Linear Collider (CLIC). They have a different energy reach, which leads to a different choice of technology. Both machines are being developed by international collaborations. The choice which machine to build eventually will depend on physics requirements, but also on technical maturity at the moment of decision and cost. [6]

## 1.2 Introducing the CLIC Project

The CLIC study at CERN aims at showing the feasibility of a normal conducting multi TeV electron-positron linear collider with a high accelerating gradient of 100MV/m. The CLIC layout is presented in figure 1.1.

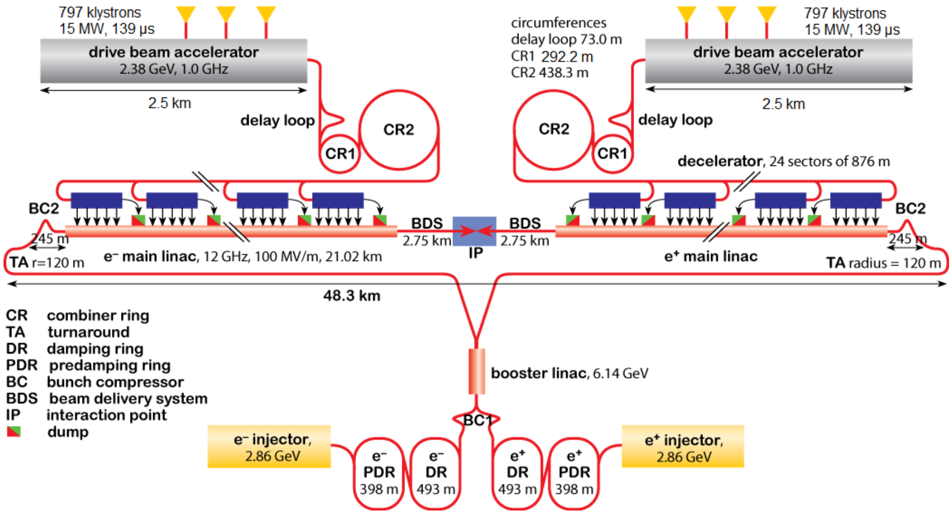

Figure 1.1: The current CLIC layout relies on two colliders facing each other resulting in a overall length of about 48.3 km.

The required technology to collide electrons and positrons at energies ranging from 0.2 TeV up to approximately 3 TeV has been developed within the CLIC study. If successful, CLIC might become the next significant particle physics facility after the LHC. Like the name suggests, CLIC is based on a linear accelerator units. Figure 1.2 shows the concept with the main components such as Accelerating Structures (AS), Power Extraction and Transfer Structures (PETS) and quadrupoles. A more detailed 3D view is presented in annexes *A* and *B*. This will eventually lead into a 48.3 km overall unit length including numerous modules with a different technical systems. The CLIC module is a high precision assembly exposed to varying thermal fields in the accelerator caused by the ramp up and operation. Like the LHC, CLIC is supposed to be located underneath the surface, which will result in more stable behaviour of the accelerating components and minor radiation effects. Yet, the final construction faculty for CLIC remains open. [8]

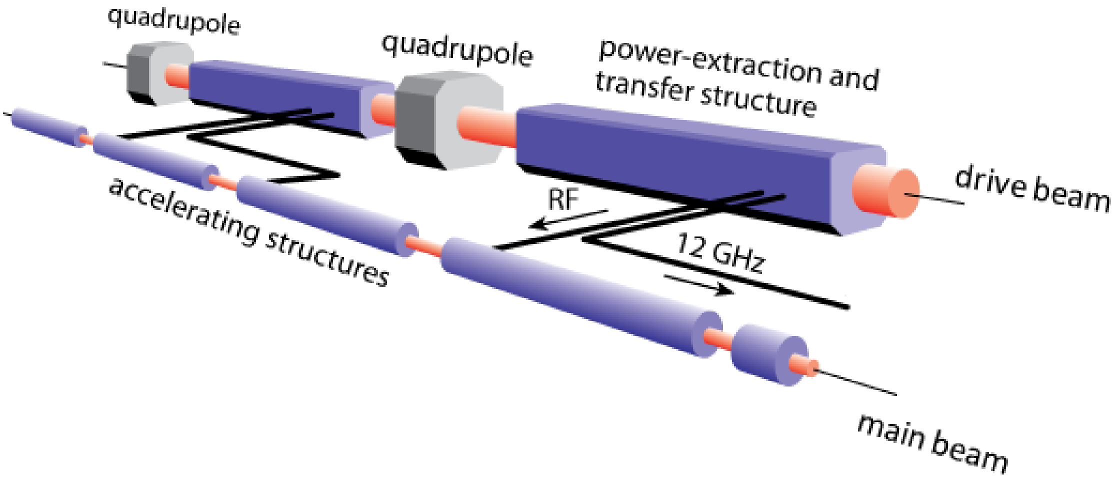

Figure 1.2: The CLIC Two-Beam scheme. The power to the main beam (MB) is provided by a secondary drive beam (DB).

CLIC is a multi-TeV normal- conducting electron- positron collider with the X-band microwave power supplied by a secondary electron parallel Drive Beam (DB). The layout relies on transforming the high current intensity and low energy from the DB into a low current but high energy Main Beam (MB). The MB passes through AS, where the beam is accelerated by the RF-power created in PETS and transferred through RF network, constituted of RF components and waveguides (WG). In the present layout, a repetitive radio frequency $f_{RF}$ of 12 GHz is used for the RF-power. The beams are focused with quadrupole magnets, which are situated along the whole length of the linear accelerator (LINAC). The quadrupoles have a significant effect on the collision intensity, i.e on the luminosity. As target, the luminosity for the current layout is 5.9 x $10^{34}$ $\frac{1}{cm^2 s}$ [9]. The so-called CLIC two-beam modules contain therefore the needed RF-components and all technical systems, such as alignment and beam instrumentation.

## 1.3 Research Methodology and the Structure of the Thesis

In this thesis, the Thermo-Mechanical Model (TMM) for the full scale CLIC module is presented using Finite Element Method (FEM). The studied CLIC module is the one finalized for the Conceptual Design Report (CDR). The thesis focuses on the thermo-mechanical effects caused by the RF-power, which are a high importance in developing the future CLIC module generations. Due to the current complexity of the modules, the modelling was implemented in steps - from geometrical simplification and model creation to the module assembly and finally towards thermo-mechanical simulations through various preprocessing phases. The modelling is strongly related to the module cooling concept, which is based on a distributed cooling by water. The simulation is considered as coupled including elements from fluid dynamics and heat transfer to structural mechanics with various contact and support definitions. Therefore, the structure of the thesis relies on the implementation of such an analysis above all. The modelling was implemented using ANSYS Workbench 13.0 software and CATIA 3D.

The main CLIC components are presented and the main function of each element is introduced during the operation. Furthermore, the origin of the applied thermal and structural loads in TMM are discussed. A short overview is presented of the alignment requirements is presented. The main objective focuses on the modelling principles formulating both the mathematical and geometrical simplifications made for the CLIC two-beam module. Both thermal and structural conditions are then introduced. Finally, the results based on the module input are presented in different operations modes. The thesis presents the modelling principles and results for a so-called standard type of the CLIC two-beam module - usually referred as type 0 module - which presents the most common module configuration in CLIC. Other type of configurations may then be assembled from this one using the same methodology presented here. In the discussion part the results and the modelling approach is evaluated. Also the accuracy of the used methodology is examined more closely.

# 2. CLIC TWO-BEAM SCHEME

For the TMM, the complex CLIC two-beam modules, having an overall length of about 2-m each, consists of three main subsystems: MB, DB and vacuum system assemblies. The CLIC type 0 includes four PETS, two Drive Beam Quadrupoles (DB Q) and eight AS mounted on alignment girders. The girders are attached to the so-called cradles, which serve as articulation points to adjacent girders. By using high precision linear actuators as a kinematic stand for the cradles, the final alignment can be achieved for the RF structures. The estimated thermal dissipation into the RF structures and magnets of a type 0 CLIC module is about 6.9kW (3.45kW/m)[10]. The main thermal contributions comes from of AS, PETS and WG when the accelerator is ramped up to its nominal level.

## 2.1 Accelerating Structures

The design of the CLIC AS is based on OFE copper disks, which are connected to each other using diffusion bonding under hydrogen at above 1000 °C. [11] The beam to be accelerated travels through the iris located in the middle of each disk. A typical copper disk for the AS is shown in figure 2.1

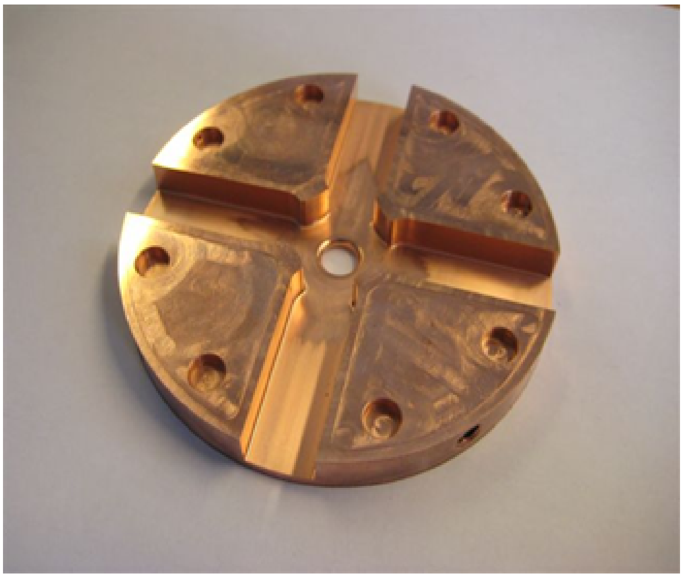

Figure 2.1: AS consists of copper disks, which are bonded together at near copper melting point.

Once the AS disks are bonded, they will be assembled together with other AS components such as the vacuum manifolds, input waveguides and cooling circuits. An illustration of the AS unit design is presented in figure. 2.2. [13].

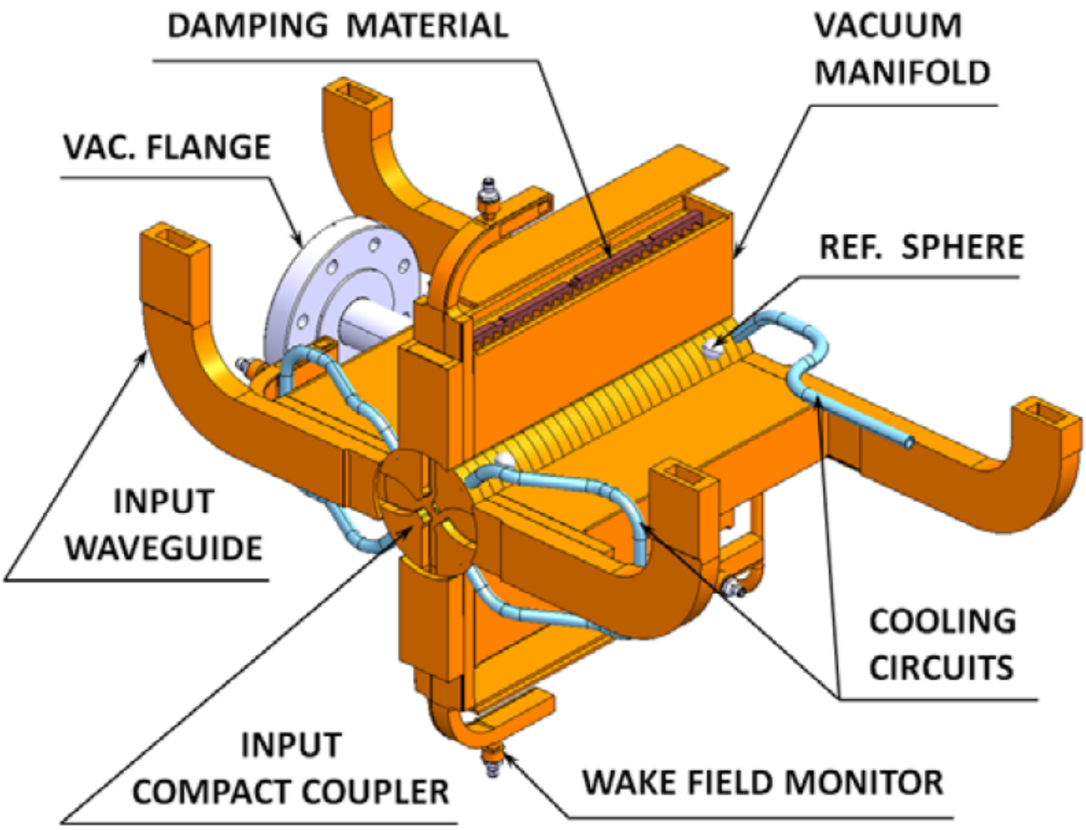

Figure 2.2: 3D illustration of AS including copper disks and vacuum contacts to other module structures.

In the two-beam acceleration scheme the RF field created by the DB is transferred to MB AS and due to differences in structure volume and shunt impedance the AS RF field is compressed from DB RF field. This AS RF field then accelerates the electron bunches by an integral number of RF periods spaced bunches in the AS. In order to have continuous acceleration the incoming electron bunches has to be in phase with the RF fields. A schematic view of the RF accelerating cavity is presented in figure 2.3. In CLIC, the AS is composed of copper slots. The shown accelerating process continues down the LINAC. [12]

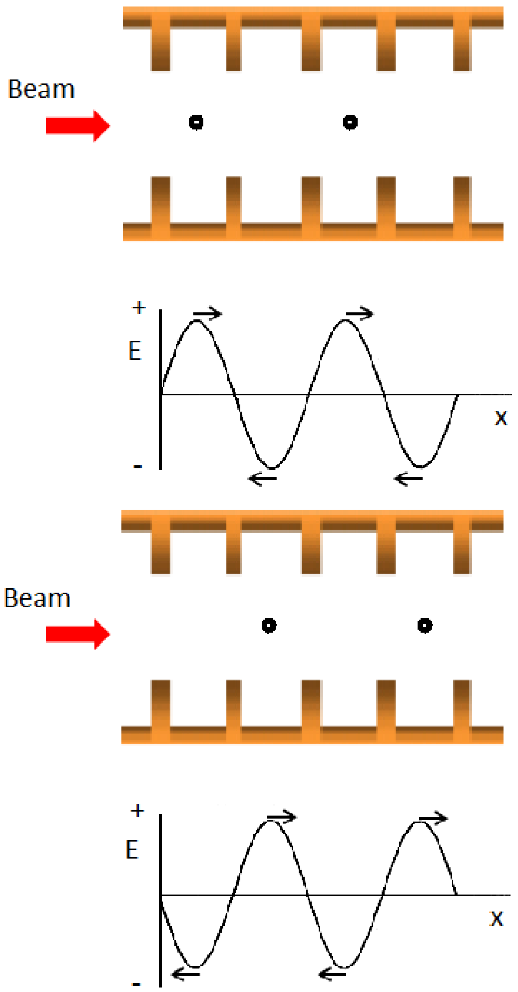

Figure 2.3: Scheme of the RF accelerating cavity for an electron bunch.

The CLIC AS must fulfil a set of demanding performance criteria, which are strongly coupled to one another in order to arrive at a high performance linear collider design. [14] Since the designed lifetime of CLIC is 20 years, the structures should tolerate also a cyclic thermal loading, which origins from the varying RF field. The RF currents causes cyclic thermal stresses on the AS, which are expect to have an impact on the material behavior through surface damage by fatigue.[15] The RF power is supplied into the AS, wherein the accelerating cavities are located. The beam bunches are accelerated by an electric field, which is oscillating sinusoidally once the RF power is being changed. Therefore, AS must be aligned to a certain accuracy in order to avoid any harmful effects on the beam. Since the accelerating structures are exposed to variable electromagnetic field governed by the structure parameters, two separate modes can be pointed out for further studies - unloaded (no beam) and loaded (beam) cases.

During the operation, the beam pulse follows a certain timing interval. The pulse consist of rising time $t_r$, filling time $t_f$ and beam time $t_b$. It should be noted that the beam time occurs only when the beam is present. The pulse lenght is fully defined by given parameters. The beam pulse shape is shown in figure 2.4. [16]

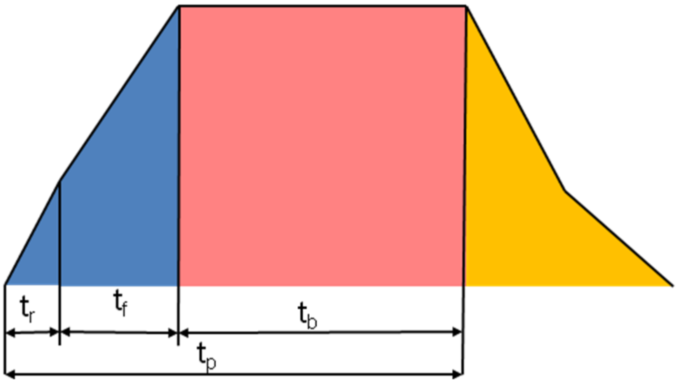

Figure 2.4: Pulse shape illustrating the beam duration on a bunch.

The main accelerating structure parameters based on the beam physics and physics requirements are presented in table 2.1. The parameters are shown for the optimized CLIC_G structure. [9]

Table 2.1: The main parameters for the CLIC accelerating structures.

| Parameter | CLIC_G |
|---|---|
| Frequency: $f$ [GHz] | 12 |
| Average iris radius/wavelength $<a>/\lambda$ | 0.12 |
| Input/Output iris radii $a$ 1.2 [mm] | 3.15, 2.35 |
| Input/Output iris thickness: $d$ 1.2 [mm] | 1.67, 1.00 |
| Group velocity: $v_g$ (1.2)/c | 1.66,0.83 |
| N. of reg. cells, str. length: $N_c$, l [mm] | 24, 229 |
| Bunch separation: $N_s$ [rfcycles] | 6 |
| Luminosity per bunch X-ing. $Lb$ x [m-2] | 1.22 x $10^{34}$ |
| Bunch population: $N$ | 3.72 x $10^9$ |
| Number of bunches in a train: $Nb$ | 312 |
| Filling time, rise time: $t_f$, $t_r$ [ns] | 62.9, 22.4 |
| Pulse length: $t_p$ [ns] | 240.8 |
| Input power: $P_{in}$ [MW] | 63.8 |
| Max. surface field: $E_{surf}$ max [MV/m] | 245 |
| Max. temperature rise: $T_{max}$ [K] | 53 |
| Efficiency: $\eta$ [%] | 27.7 |
| Figure on merit: $\eta Lb$ x $/N$ [a.u.] | 9.1 |

Together with the beam pulse behavior an average thermal dissipations can be calculated for each section and component by using the following equations.

$$P_{dissipated}^{unloaded} = (P_{in}^{unloaded} - P_{out}^{unloaded}) \cdot t_p \cdot f_{rep}, \tag{2.1}$$

$$P_{dissipated}^{loaded} = (P_{in}^{unloaded} - P_{out}^{unloaded}) \cdot (t_r + t_f) \cdot f_{rep} + (P_{in}^{loaded} - P_{out}^{loaded} - P_{beam}^{loaded}) \cdot t_p \cdot f_{rep}, \tag{2.2}$$

$$P_{beam}^{loaded} = P_{in}^{loaded} \cdot \eta \cdot \frac{t_p}{t_b}, \tag{2.3}$$

where $f_{rep}$ and $\eta$ indicates the repetition frequency and efficiency, respectively.

Finally, the thermal dissipations for the AS can be calculated for unloaded and loaded operation mode. In loaded case the dissipated heat into the AS iris is smaller since part of the beam energy is transferred to the beam. The main parameters are shown in table 2.2

Table 2.2: Beam parameters including the amount of thermal dissipation on each operation mode.

| Operation point | Power dissipation [W] | Power to the load/beam [W] |
|---|---|---|
| Unloaded condition | 410.6 | 357.6/- |
| Loaded condition | 336.2 | 219.2/212.8 |

## 2.2 Power Extraction and Transfer Structure

"The PETS is a passive microwave device in which bunches of the drive beam interact with the impedance of the periodically loaded waveguide and excite preferentially the synchronous mode. The RF power produced is collected at the downstream end of the structure by means of the Power Extractor."[9]. The energy produced during deceleration is transferred from low energy and high intensity DB to the AS. In the current layout, the single PETS should produce RF power for two AS. PETS are composed of copper octants separated by damping slots. Typical PETS octants are shown in figure 2.5. The octants are jointed together and assembled afterwards into a complete PETS with RF and vacuum sub-assemblies.

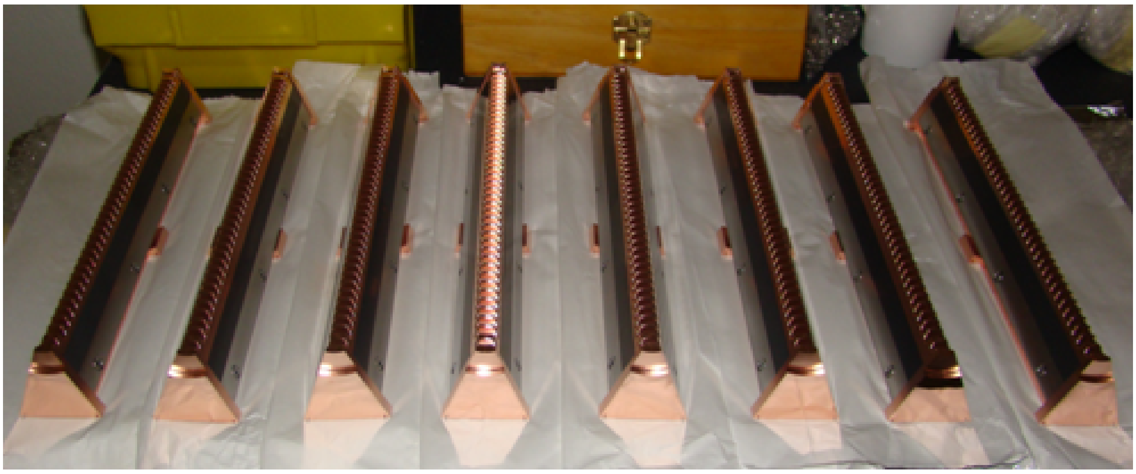

Figure 2.5: PETS are constructed from copper octants, which are jointed together for further assembly.

More complete illustration of a PETS unit is shown in figure 2.6. In TMM point of view, PETS has two types of thermal losses: surface currents and steady-state losses by the beam. It can be assumed that the surface currents induce an uniform heat dissipation into the PETS. The heat loss is not constant along a beam sector but for the TMM cooling estimation the highest value was used for the whole sector.

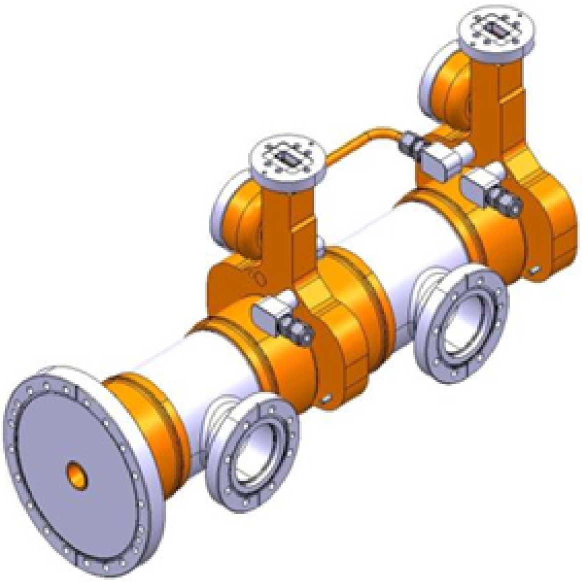

Figure 2.6: 3D view of a complete PETS unit.

The second source of thermal dissipation, steady-state beam losses, are not uniform but increases alongside the energy spread. Therefore it was assumed that the cooling system should cope with 0.5 % of the beam power integrated through a drive beam sector while the beam loss is 0.1 % in the beginning of a sector. Further, because beam loss increases when beam energy and current decreases through a drive beam sector, we assumed that the beam losses follows a parabolic distribution along DB sector. After obtaining the distribution that fulfils the 0.5 % of integrated beam loss dissipation, the maximum value of the obtained dissipation in a sector was selected for the cooling requirement including a safety factor of three. Together with the accelerating parameters, the average power dissipation for each component can be expressed. The decelerator parameters are shown in table 2.3. [9]

Table 2.3: Decelerator parameters.

| Decelerator parameters | Notation | Value | Unit |
|---|---|---|---|
| No. of drive beam sectors linac | $N_{unit}$ | 24 | - |
| Unit length (total) | $L_{unit,total}$ | 868 | m |
| No. PETS / sector | $N_{PETS,unit}$ | 1491 | - |
| Length of PETS (active/overall) | $L_{PETS}$ | 0.213 | m |
| main beam acceleration power / PETS | $P_{acc}$ | 2 x 63.9 | MW |
| Main beam energy gain | $\Delta E_{main}$ | 62.5 | GeV |
| Drive beam RF efficiency | $\eta_{decRF}$ | 65 | - |
| PETS tolerance | | 31 | $\mu$m |
| Energy (decelerator injection) | $E_{in,dec}$ | 2.38 | GeV |
| Energy (final, minimum) | $E_{fin,dec}$ | 238 | MeV |
| Average current in pulse | $I_{dec}$ | 101 | A |
| train duration | $\tau_{train}$ | 241.4 | ns |
| RF frequency | $f_{RF}$ | 12 | GHz |
| No. of bunches / train | $N_{b.dec}$ | 2904 | - |

The shape of the dissipated steady-state beam loss is shown in figure 2.7. For the TMM the maximum value was considered. [17]

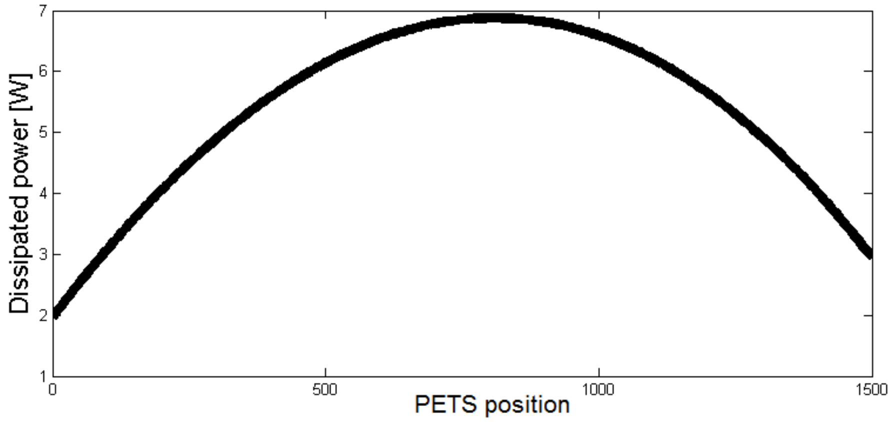

Figure 2.7: The steady-state beam loss follows a parabolic shape.

In table 2.4 the total thermal dissipation for the PETS is shown with beam loss and surface current loss.

Table 2.4: Thermal dissipations for the PETS including a dedicated safety factor.

| PETS [W] | Thermal dissipation [W] | Including margin [W] |
|---|---|---|
| Beam loss (steady-state) | 7 | 21 |
| Surface current | 22.4 | 67.2 |
| Total | 29.4 | 88.2 |

## 2.3 Quadrupole Magnets

The CLIC two-beam module includes two DB Q. Total, both decelerators will include 41400 quadrupoles resulting in the most common type of magnets of all the CLIC complex. The current design proposes working gradient of 81.2 down to 8.12T/m. [19] According to CDR, DB Q will be located at constant spaces along the decelerators. Figure 2.8 shows the main elements in DB Q. The vacuum chamber is connected to the DB Q as well as to the PETS located on both sides of the magnet. The BPM (Beam Position Monitor), whose purpose is to monitor the beam and consequently adjust the DB Q, is situated between the magnet and the PETS.

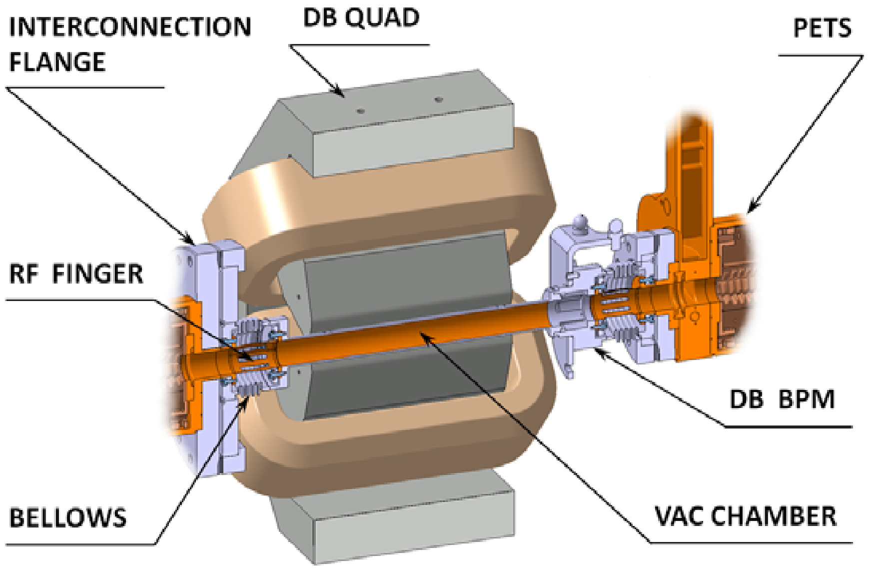

Figure 2.8: DB Q with its the main elements as well as its interconnection to the adjacent components.

From the TMM point of view, the DB Q is taken into account but only through its gravitational effects. The magnet poles are thermally insulated from the coils and thus, the heat loss generated in the coils is assumed to have insignificant effect on the interconnected components, e.g. the DB drift tube. For the DB Q, a steady-state temperature rise in the magnet coils is considered based on the manufacture cooling specification. The maximum temperature rise in coils should not exceed 5°C. [18]

## 2.4 Vacuum System

The vacuum envelope used in the CLIC layout is mainly composed of the RF system. The vacuum requirement is $10^{-9}$ mbar. It should be noted that the vacuum should cover the whole length of the beam pipe which is shown in figure 2.9. [19]

For the vacuum modelling, the effect of the vacuum condition was taken into account by applying a negative atmospheric pressure on internal vacuum surfaces on the RF network and vacuum network between MB and DB having significantly the largest surface area exposed to vacuum condition. No vacuum condition were applied on the internal surfaces of AS or PETS. The vacuum caused effect on the AS and PETS can be better simulated using a smaller model specifically developed for such a analysis.

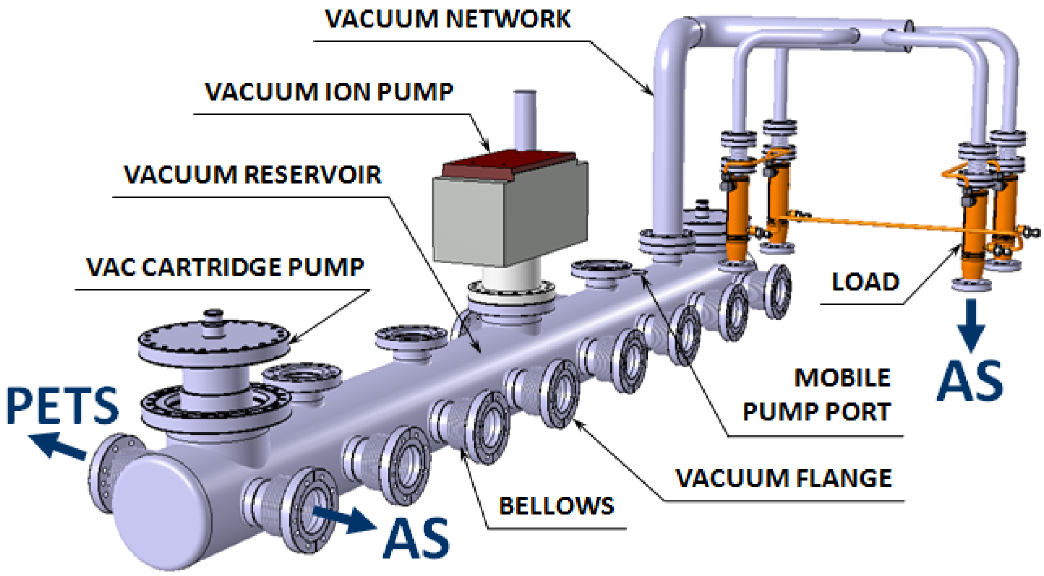

Figure 2.9: Vacuum reservoir illustrating the main interconnections into MB and DB.

The vacuum network is connected to the MB and DB side through flexible bellows. Bellows have two different kind of orientation; horizontal and vertical. Vertical contact for the bellows is used only for the loads.

## 2.5 RF Network

The CLIC two-beam module RF network mainly consists of water cooled WG, CMF (Choke Model Flange) and loads. The RF network has also several other subcomponents such as the PETS On-Off mechanism, which transmits or reflects the needed RF power from the PETS into two adjacent AS. [20] In the RF chain, the CMF permits to move and align the DB and MB separately. It also provides an electrically contact-free connection between the waveguides. The RF network is illustrated in figure 2.10.

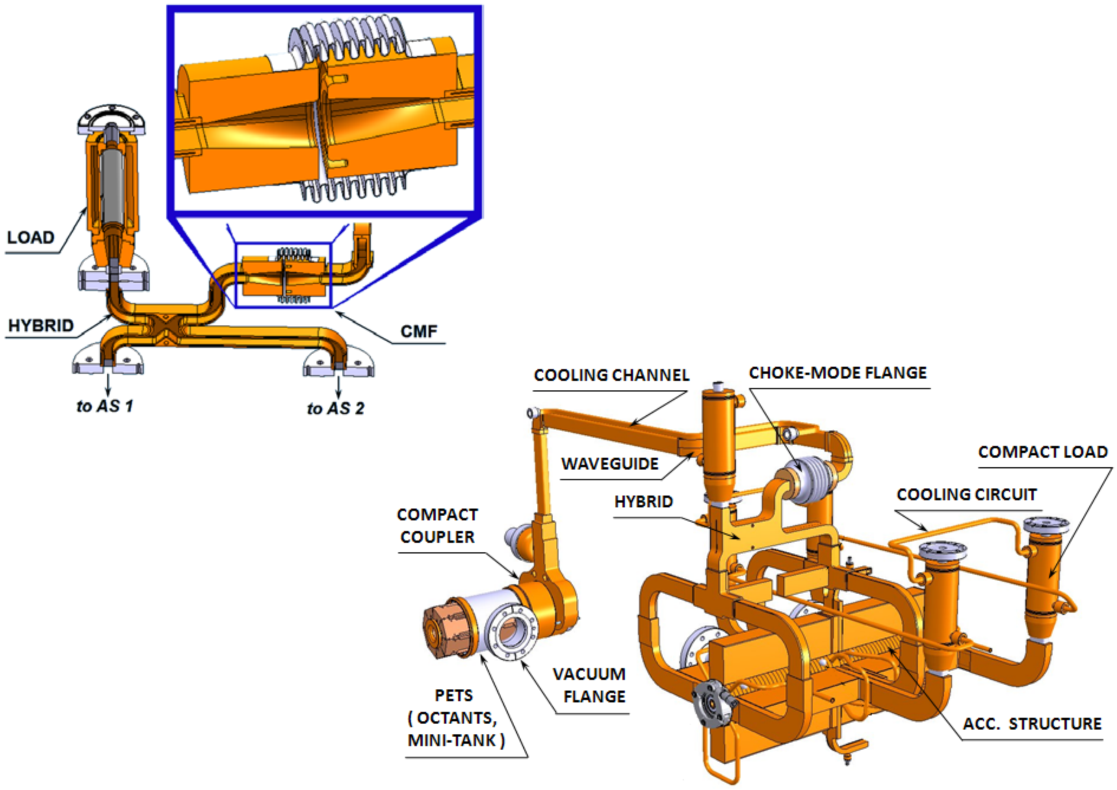

Figure 2.10: The RF network creates the link between the DB and the MB enabling the RF power transmission.

Since the RF power is transmitted from PETS to AS via WG, the WGs are exposed to thermal dissipations. For the RF-network, a loss parameter was defined: 0.7 % of the PETS output power. Assuming current parameters, this corresponds to 11 W per waveguide feeding RF power to the MB.

## 2.6 Cooling System

Most of the power loss in CLIC is seen as heat dissipation on the RF structures. Therefore, an effective cooling system is required to extract the generated heat. The current CLIC two-beam module cooling is based on distributed water channels. The Super AS (SAS) are cooled in parallel whereas the PETS and waveguides are cooled in series. The cooling system corresponding the current CLIC module layout is shown in figure 2.11. The water is pumped into the module at temperatures to avoid condensation in the tunnel environment. In the current cooling scheme, the water inlet temperature is 25 ° C and the cooling is based on fully turbulent flow, in where the flow has more vortexes, to ensure an efficient heat transfer environment.

The aim is to regulate the flow such that the output temperature of the water

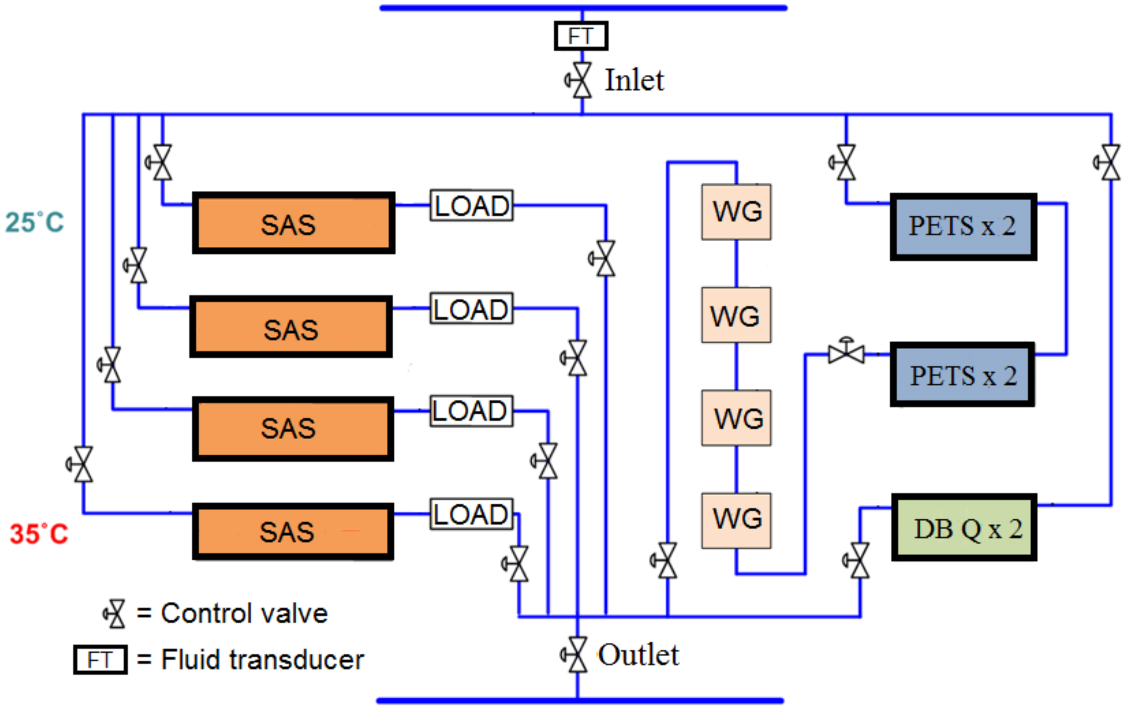

Figure 2.11: The CLIC module cooling scheme.

can be controlled and thus structure temperature can be levelled and sustained at design values in all linac operation conditions. This requires excellent input water temperature stability as well as a feasible range for the flow regulation in the cooling system.

## 2.7 Supporting and Alignment System

The micro-precision CLIC structures will be supported and aligned on so-called girders. All girders are mechanically interconnected constituting a so-called snake system. This system allows for the precise alignment on the overall length of the two linacs. The girders are then position monitored and re-aligned. A fundamental issue of the proper operation of the snake system is the stiffness of the girders and the V-shape supports. It is expected that the girders and the V-shape supports will have higher stiffness values in comparison with other components of the CLIC two-beam modules. Therefore, the possible static deformation of the girders and the V-shaped supports are taken into account at an earlier stage, while calibrating the actuators. The most critical contributions will be directed to the AS and PETS. [21, 22]

In figure 2.12 the V-shape support, which creates the interconnection between the RF structures and the girders is shown. The tolerance for the beam axis is defined as a cylinder with 10 $\mu$m tolerance on its diameter. Longitudinally the V-shape support should have a positioning within 0.5 mm with respect to alignment requirements. [23]

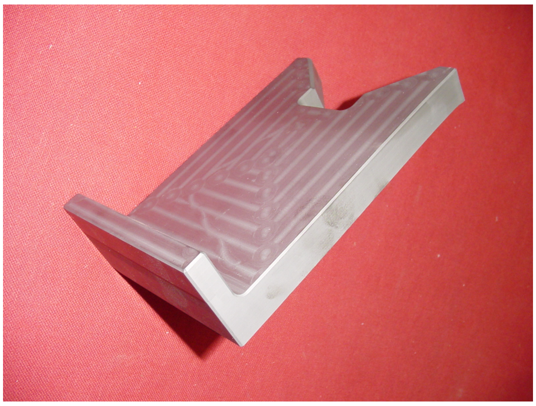

Figure 2.12: V-shaped silicon carbide support.

Figure 2.13 shows the method to calculate the V-shape supports tolerance.

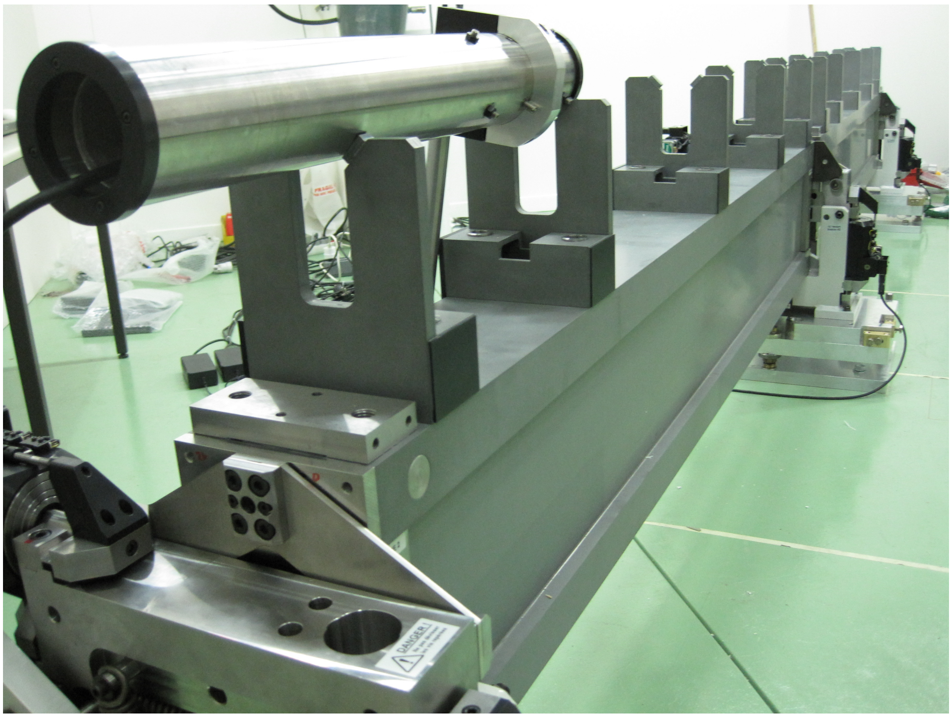

Figure 2.13: Supporting system qualification in a dedicated laboratory.

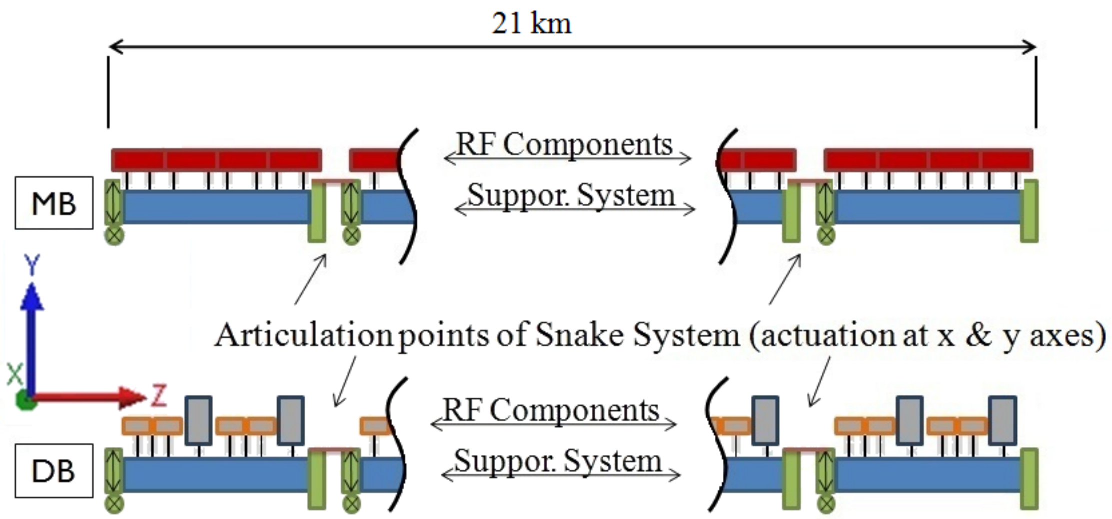

Figure 2.14: Supporting system for the MB and DB RF components.

The baseline scheme of the supporting system is shown in figure 2.14. The choice of the girders is of prime importance. Few girders are currently manufactured made of silicon carbide (SiC). For the time being, also an alternative material, newly developed, Epument mineral cast, has been chosen as a possible candidate. The main girder requirements are shown in table 2.5. The d.o.f (degrees of freedom) for the supporting actuators are $x$, $y$ and rotation about the $z$ axis. During the CLIC module operation, the alignment between different operation modes must be controlled at a micrometer level. [24]

Table 2.5: The main mechanical requirements set for the CLIC MB and DB girders

| Parameter | Requirement |
|---|---|
| Modulus of elasticity | $> 400$ GPa |
| Mass per girder | $< 240$ kg |
| Max. vertical deformation in loaded operation | 10 $\mu$m |
| Max. lateral deformation in loaded operation | 10 $\mu$m |
| Max. weight on top of the girder | 400 kg/m |

As AS, PETS are aligned separately, the connections between them need to be flexible. However, the vacuum should be uniform over all the structures. According to the developed supporting scheme, up to eight AS are mounted on a girder. The structures are aligned with respect to each other on the girder, which forms a subsystem for the active alignment system. Then the girders are aligned with respect to the beam.

From the TMM point of view, the main interest regarding the stability of the CLIC module focuses on the RF structures, namely AS and PETS. In table 2.6 the main alignment requirements are shown. [19] The alignment includes pre-alignment and beam based alignment.

Table 2.6: The main alignment requirements for CLIC two-beam module

| Structure | Tolerance [$\mu$m] |
|---|---|
| AS | 14 |
| PETS | 31 |
| AS-WFM | 5 |
| Structure-BPM | 10 |

The, tolerances denoted as AS - WFM (Wake Field Monitor) and DB Q - BPM are relative tolerances for the beam based alignment. The reason why the relative tolerances have been introduced is that the relative position of the structures is the foundation of the beam based alignment strategy. Harmful effects induced in the beam can be minimized with respect to the reading of the WFM and BPM if they are positioned accurately enough according to the corresponding AS and magnets, respectively. At the moment, these are the tolerances of the CLIC structures and components, which the supporting and alignment systems has to achieve. [21]

# 3. THERMO-MECHANICAL MODEL DESCRIPTION

## 3.1 Geometry

The TMM was built according to the CLIC CDR baseline module design and includes all main RF structures and components with the supporting systems. The geometry was created in Catia and then implemented into ANSYS Design Modeller as an ascii format (*stp.). A 3D view of the geometry used in TMM is shown in figure 3.1.

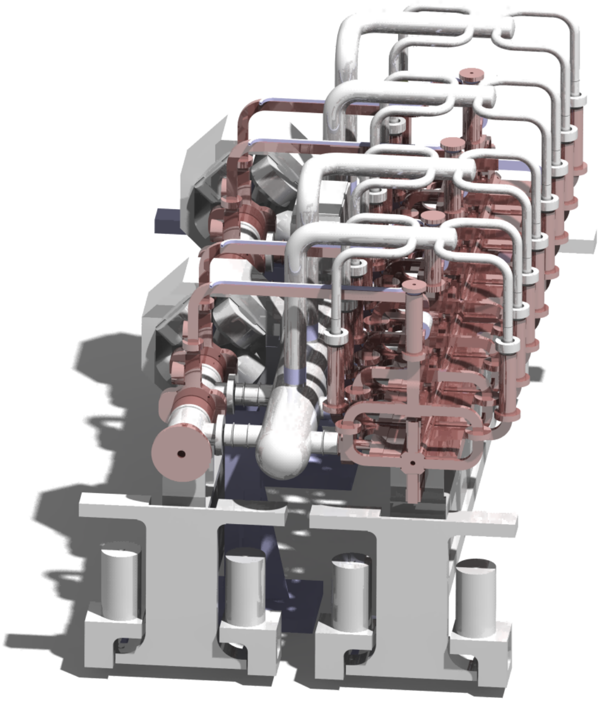

Figure 3.1: A 3D illustration of the CLIC two-beam module built and simplified in Catia.

The created 3D models in CAD system were used as a baseline in TMM. Each assembly component was simplified one by one in order to have a suitable and feasible model for later analysis. The simplification included suppression of geometrical features such as fillets and chamfers. Also the cooling channels inside each AS and PETS were remodelled, due to the non trivial fluid flow modelling presented below.

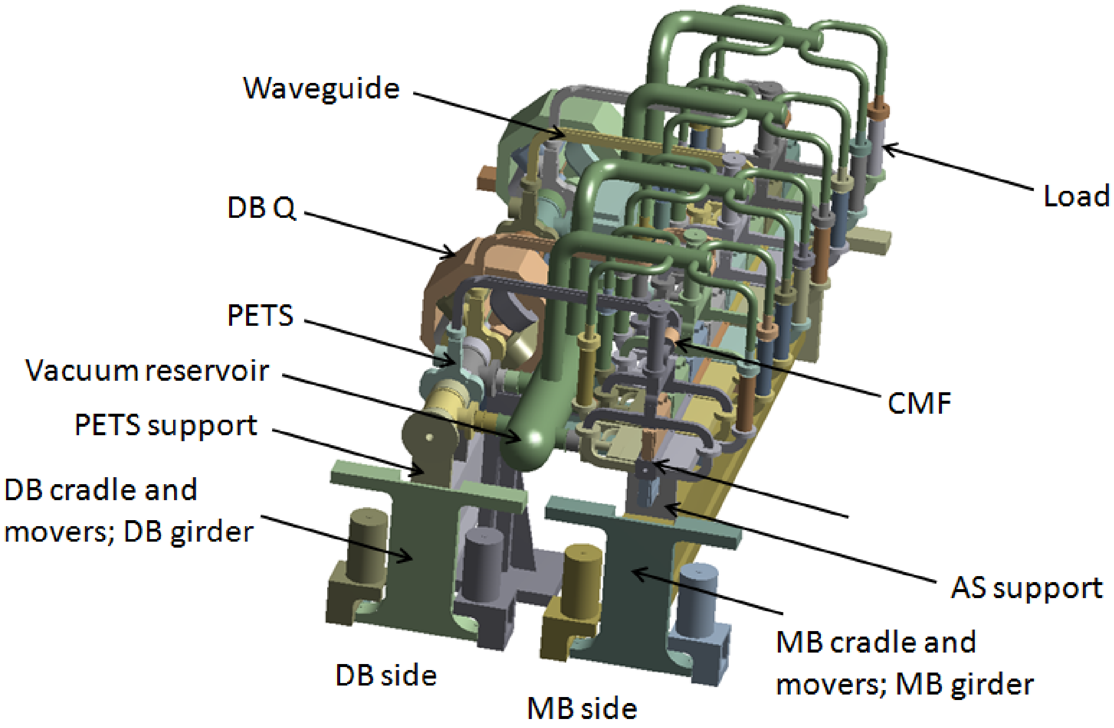

Figure 3.2: The main components included to the TMM corresponding the CLIC module.

During the simplification, the sub-components were imported into ANSYS for further studies especially regarding the meshing controls. Each part was considered as simplified when an appropriate meshing was obtained. Finally, the sub-assemblies were imported into ANSYS for pre-processing and further TMM. The main components included in the FEM model are shown in figure 3.2

The overall optimized model consists of more than 1000 parts. From the TMM point of view, the CLIC module geometry consists of MB, DB and vacuum system assemblies. This separation is done to ensure flexible vacuum connections between the subsystems to enable independent beam alignment. In addition to the main components, the geometry also takes into account beam pipes, waveguides and supports. The waveguides are aligned between the interconnection from PETS to AS. The main component materials used in the model are copper OFE (RF structures), silicon carbide (supports) and stainless steel (vacuum components).

## 3.2 Inputs and Assumptions

The simulation environment which was created for the TMM coupled fluid dynamics, heat transfer and structural physics. In this case steady-state thermal and static structural simulations were considered. For transient response, the model would require numerous substeps increasing the computation time up to unacceptable level.

To obtain the TMM responses ANSYS 13 Mechanical was chosen as a platform. To obtain the thermo-mechanical responses of the CLIC module the following inputs and assumptions were considered:

- Thermal loads into the RF structures;
- Current module geometry including the real supporting system;
- AS brazed together as one solid structure;
- SAS interlinked via bellows;
- MB and DB girder supports fixed to the ground;
- Vacuum reservoir fixed to the ground;
- Vacuum reservoir directly connected to the RF structures with flexible bellows;
- Both fixed and sliding contacts between components;
- Natural convection of heat to the air.

The thermal loads into RF structures composes of AS, PETS and WG. The RF structures are thermally coupled and thus, loading in one structure has influence into another. For the AS the loading varies depending on the operation mode. Furthermore, the loading is not uniformly distributed along the beam line. The difference between operation modes is mainly due to the thermal load on the MB side. In both unloaded and loaded modes the gravity and vacuum load are the same. The ambient temperature was considered to be at 30° C.

Inside the AS, PETS and WG, the dissipated heat is transferred to the coolant via convection. For this a separate convectional area was created for each component using ANSYS named selection grouping. An illustration of the AS convectional area is shown in figure 3.3.

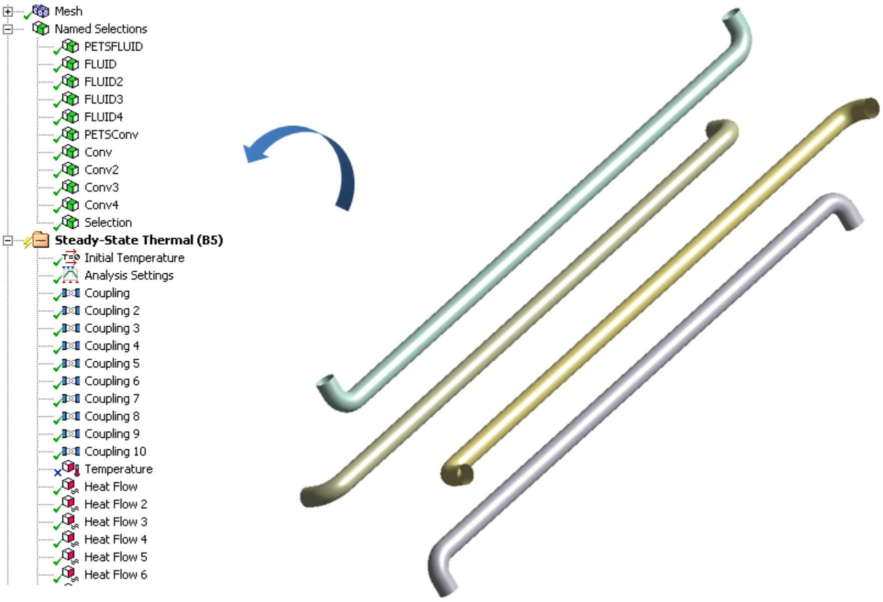

Figure 3.3: Inner illustration of the convectional area created inside the cooling conduct for the coolant water flow.

Similarly, the vacuum surface are created using Ansys named selections. The vacuum condition is applied mainly for the vacuum reservoir and network areas shown in figure 3.4. The applied pressure variation inside the components and the surrounding environment is 1 bar, which causes a load condition to the module together with thermal and gravitational effects.

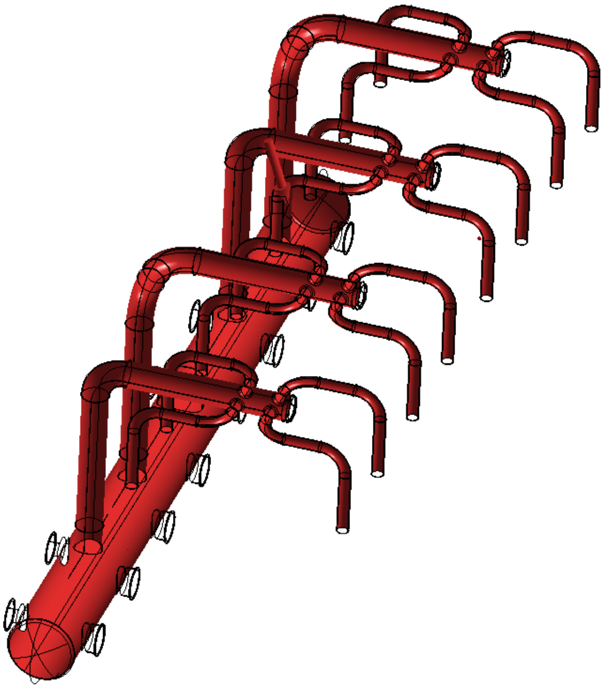

Figure 3.4: Illustration of the main surfaces where a vacuum condition is applied in TMM.

In order to maintain mechanical stability and alignment, the module supporting system is defined as shown in figure 3.5. The TMM was created so that it includes all the essential supports for the RF components and girders. In the supporting design, especially the vacuum and RF caused effects were taken into account. First of all, the RF structures are supported on the V-shape supports so that both fixed and sliding boundary conditions are used. By using both fixed and sliding supports for the RF structures, the thermal expansion can be divided in parts. Moreover, the interconnections include several bellows, which decrease the thermal effects even more. The flexible contacts between the vacuum network and MB/DB side also decreases the vacuum caused structural effects.

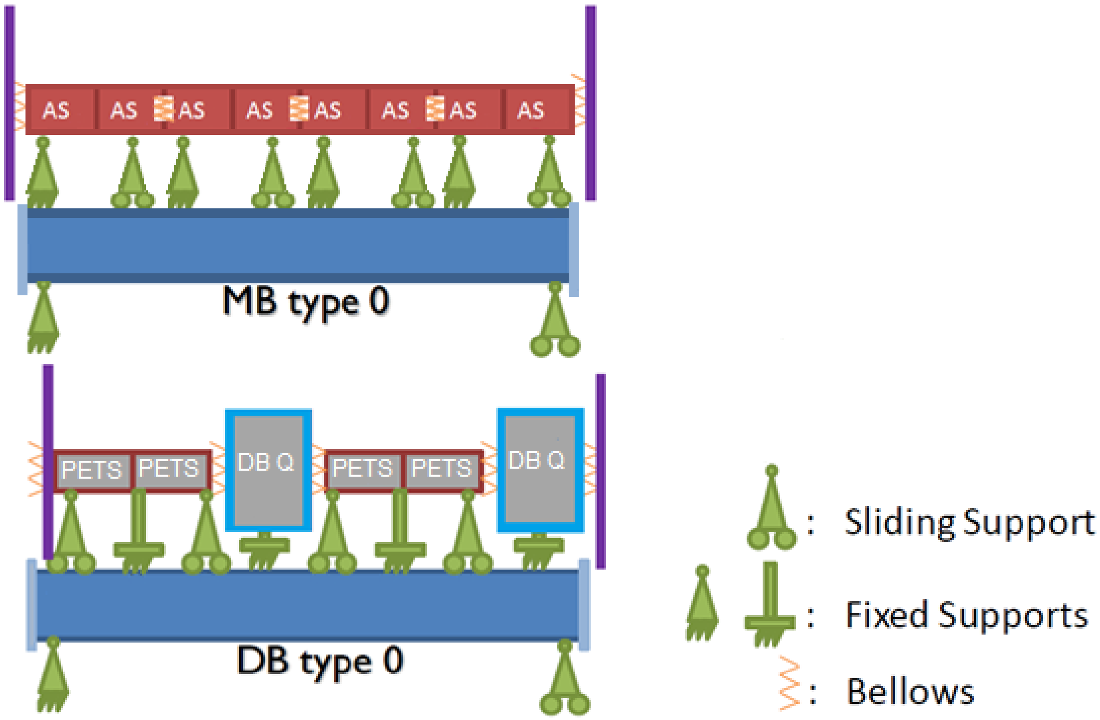

Figure 3.5: The CLIC two-beam module structural boundary conditions. SAS and PETS are interlinked one into other using bellows. For the V-shape supports both fixed and sliding boundary conditions were used.

## 3.3 Load Conditions

The induced thermal loads are an essential part of the operation of the CLIC and an efficient cooling based on the parameters shown in table 3.1 is an essential part of the design.

Table 3.1: TMM cooling boundary conditions. HTC: heat transfer coefficient

| Item | Description | Value |
|---|---|---|
| Input flow MB | mass flow (unloaded) | 68.6 kg/h |
| Input flow MB | mass flow (loaded) | 56.2 kg/h |
| Input flow DB | mass flow | 37.4 kg/h |
| Water input | temperature | 25 °C |
| HTC MB | convection to water | 5079 W/($m^2$ K) |
| HTC DB | convection to water | 1407 W/($m^2$K) |
| HTC air | convection to air | 4 W/($m^2$ K) |

The mass flow rates has been defined resulting equal water temperature rise of about 5°C in AS in both unloaded and loaded operation. The current TMM loading parameters are based on the average heat dissipation. The total input power for the

CLIC module is about 3.49 kW and 2.89 kW in unloaded and loaded operations, respectively. The most significant contributions are directed to the RF components.

The main thermal dissipations for the module components in unloaded and loaded operation are summarized in table 3.2. In the TMM, PETS and WG have constant heat loads but the AS RF load varies during the operation.

Table 3.2: Summary of the applied thermal conditions in TMM on each RF structure. The maximum heat dissipation for the module is seen in unloaded operation.

| Component | Heat dissipation | Total per module |
|---|---|---|
| AS (unloaded) | 411 W | 3.3 kW |
| AS (loaded) | 336 W | 2.7 kW |
| PETS | 39 W | 156 W |
| WG | 11 W | 45 W |

In figure 3.6 and in annex *C* the heat flux dissipation is presented for both unloaded and loaded operation mode. As seen the heat loss is quite evenly distributed in unloaded case along the AS length. In loaded, on the contrary, the loss shape has its maximum value at the beginning of each AS and is decreasing along the axis length. The net heat loss can be obtained by integrating the heat flux profile along the beam axis.

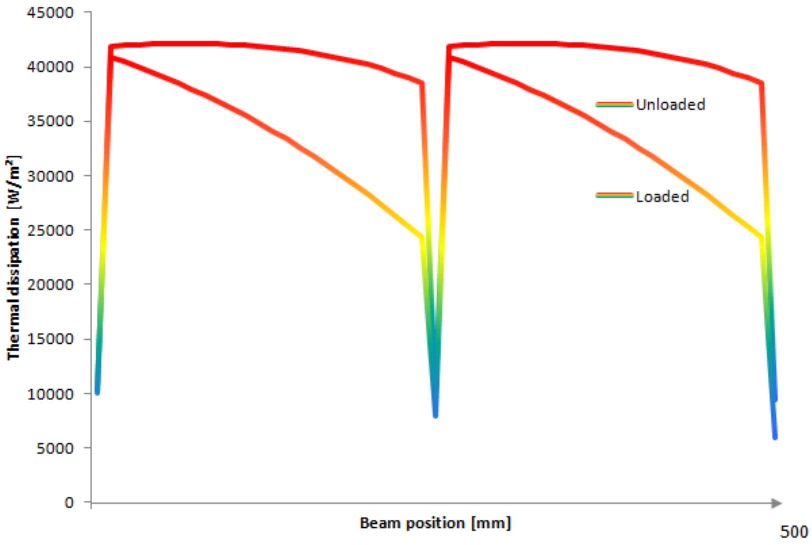

Figure 3.6: The RF dissipation in AS is not uniformly distributed along the beam axis. The unloaded overall heat integrated has its value of about 821 W for a SAS.

## 3.4 Modeling Principles

### 3.4.1 Fluid-Thermal Interface

In order to compute a solution for the module, a simplified approach was used for the fluid flow modelling. Instead of using a standard 3D CFD method, a 1D fluid-thermal elements were used and coupled with 3D solid elements. The method has been validated resulting into an equal temperature distribution as 3D CFD method with a good accuracy [25, 26, 27]. Since the fluid flow itself is not under investigation but the aim to obtain the temperature distribution, a 1D flow method can be considered applicable. The heat transfer environment between the fluid and solid elements were created separately using ANSYS Parametric Design Language (APDL) script code. For one fluid network the applied script code is presented in annex *D*. The code is applied separately on all components. With this kind of approach, the temperature distribution within the module as well as within the flowing water can be modelled and imported to structural FEA afterwords. The fluid thermal element is applied on a line inside the considered cooling pipe. Similarly, a line body with a cross section was modeled inside the accelerating structure cooling pipe. In figure 3.7 the constructed fluid network for 1D water flow is presented.

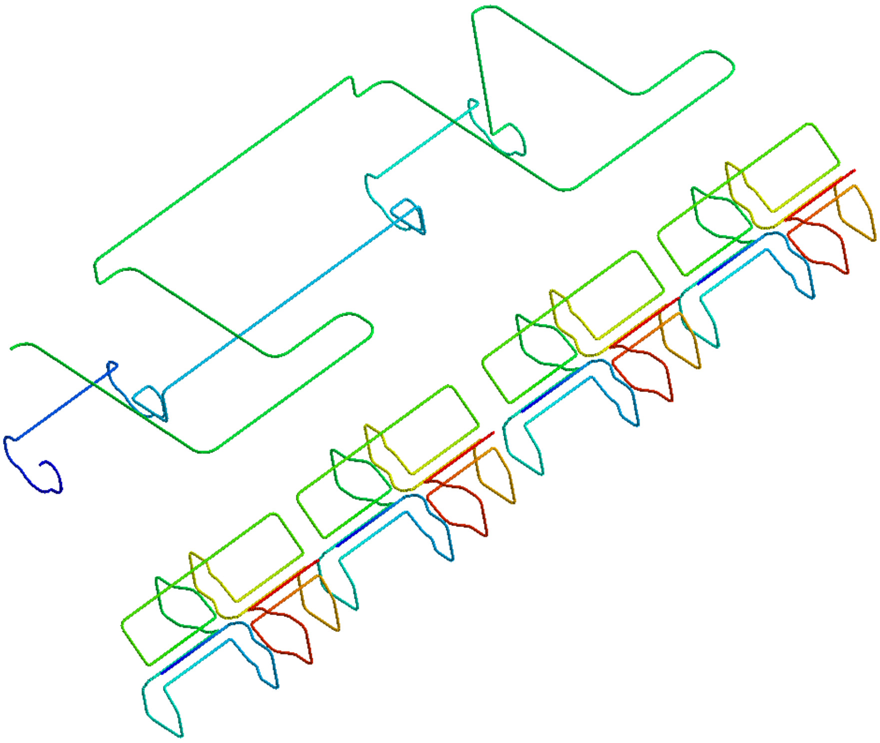

Figure 3.7: The constructed fluid network for 1D water flow in the CLIC module.

In a standard 3D fluid flow the governing equations are based on the conservation of mass (3.1) and momentum (3.2, 3.3, 3.4).

$$\frac{\partial u}{\partial x} + \frac{\partial v}{\partial x} + \frac{\partial w}{\partial z} = 0 \tag{3.1}$$

$$\rho\left(\frac{\partial u}{\partial t} + u\frac{\partial u}{\partial x} + v\frac{\partial u}{\partial y} + w\frac{\partial u}{\partial z}\right) = -\frac{\partial p}{\partial x} +$$

$$\mu\left(\frac{\partial^2 u}{\partial x^2} + \frac{\partial^2 u}{\partial y^2} + \frac{\partial^2 u}{\partial z^2}\right) + \rho g_x \tag{3.2}$$

$$\rho\left(\frac{\partial v}{\partial t} + u\frac{\partial v}{\partial x} + v\frac{\partial v}{\partial y} + w\frac{\partial v}{\partial z}\right) = -\frac{\partial p}{\partial y} +$$

$$\mu\left(\frac{\partial^2 v}{\partial x^2} + \frac{\partial^2 v}{\partial y^2} + \frac{\partial^2 v}{\partial z^2}\right) + \rho g_y \tag{3.3}$$

$$\rho\left(\frac{\partial w}{\partial t} + u\frac{\partial w}{\partial x} + v\frac{\partial w}{\partial y} + w\frac{\partial w}{\partial z}\right) = -\frac{\partial p}{\partial z} +$$

$$\mu\left(\frac{\partial^2 w}{\partial x^2} + \frac{\partial^2 w}{\partial y^2} + \frac{\partial^2 w}{\partial z^2}\right) + \rho g_z \tag{3.4}$$

where the x,y,z indicates to the space coordinates used in cartesian coordinate system, $\rho$ is the density, u,v,w are the velocity components respect to the coordinates x,y and z, respectively, p is pressure and g is the accelerating gravity. The notations $\frac{\partial}{\partial()}$ and $\frac{\partial^2}{\partial()^2}$ refer to the first and second derivatives.

The applied fluid-thermal element used is presented in Fig. 3.8 in local cartesian coordinate system.

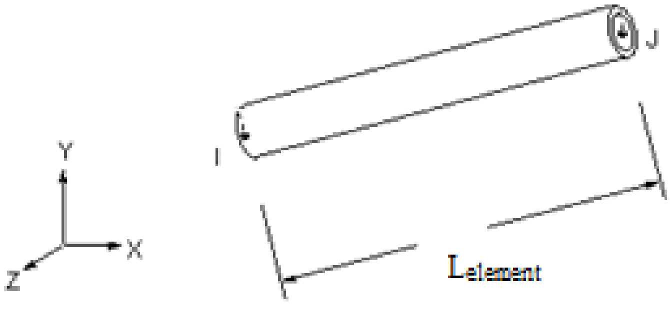

Figure 3.8: 1D fluid-thermal element illustrating the nodes I and J, which define the element length.

In 1D flow the fluid-thermal environment is coupled directly and can be expressed in form of

$$N_c \begin{bmatrix} \mathbf{C^t} & 0 \\ 0 & 0 \end{bmatrix} \begin{pmatrix} \dot{\mathbf{T}} \\ 0 \end{pmatrix} + N_c \begin{bmatrix} \mathbf{K^t} & 0 \\ 0 & \mathbf{K^p} \end{bmatrix} \begin{pmatrix} \mathbf{T} \\ \mathbf{P} \end{pmatrix} = \begin{pmatrix} \mathbf{Q} \\ \mathbf{W} \end{pmatrix} + \begin{pmatrix} \mathbf{Q^g} \\ \mathbf{H} \end{pmatrix} \tag{3.5}$$

where $N_c$ is the number of parallel flow channels, $\mathbf{C^t}$ specific heat matrix for one channel, $\dot{\mathbf{T}}$ is vector of the variations of the nodal temperature respect to time, $\mathbf{K^t}$ is the thermal conductivity matrix for one flow channel, $\mathbf{K^p}$ is the pressure conductivity matrix for one flow channel, $\mathbf{T}$ is the nodal temperature vector, $\mathbf{P}$ is the nodal pressure vector, $\mathbf{Q}$ the nodal heat flow vector, $\mathbf{W}$ is the nodal fluid flow vector, $\mathbf{Q^g}$ is the internal heat generation vector for one flow channel and $\mathbf{H}$ the gravity and pumping effects vector for one channel.

Furthermore, the energy equilibrium based on Bernoulli's law for the 1D system illustrated in figure 3.9 system can be written as

$$Z_I + \frac{P_I}{\rho g} + \frac{v_I^2}{2g} + \frac{P_{PMP}}{\rho g} = Z_J + \frac{P_J}{\rho g} + \frac{v_J^2}{2g} + C_L \frac{v_a^2}{2g} \tag{3.6}$$

where I and J are the element nodes, Z is the coordinate in the negative acceleration direction, P is the pressure, g is the acceleration of gravity, v is the velocity, $v_a$ is the additional velocity to account for extra flow losses, $P_{PMP}$ is the pump pressure and $C_L$ is loss coefficient.

Figure 3.9: An artistic view showing the main principle of a 1D flow modeling. The velocity of the coolant is fully defined with the given mass flow.

In steady-state conditions the heat dissipation can be expressed as

$$\dot{Q} = C_s \dot{m} \Delta T, \tag{3.7}$$

where $\dot{Q}$ is the dissipated heat, $C_s$ is the specific heat for water, $\dot{m}$ is the mass flow and $\Delta T$ is the temperature difference.

The effect of using 1D flow compared to 3D cases is easily shown from the above equations. Whereas the general form of Navier-Stokes equations for incompressible fluid flow represents a group of nonlinear partial differential equations [28, 29] , the utilization of FLUID116 simplifies the formalization into a single linear equation to be applied on every element node. Moreover, the solution based on 3D flow in a turbulent flow is non-trivial. In turbulence the chaotic behavior of the flow yields into an extremely difficult solutions. [30] A stable solution for turbulent flow requires fine mesh resolution, which in TMM point of view results in infeasible computation time. Obtaining the thermal response for an object of the scale of the CLIC module using a 3D flow would also yield into stability problems, because of the amount of the computation it uses during solution. By using a 1D fluid flow, the thermal simulation can be solved in considerably less time compared to 3D CFD.

Nevertheless, 3D fluid flow modelling could be taken into account for the most critical module sub-assemblies, namely for the AS. The flow speed inside the cooling channels is not uniformly distributed in reality but varies especially near the inlet/outlet areas multiplying the nominal speed of the flow considerably. Possible vibrations in the accelerating structure could therefore lead to alignment difficulties. [31] Since the 1D approach is not able to predict any force induced phenomena in the AS, more detailed simulation could be carried out. For this purpose, different kind of solution algorithms could be used such as the so-called $k\epsilon$-turbulence model, which is related to one of the most commonly used RANS (Reynold's averaged Navier-Stokes equations) models. [32] In this model two equation model k indicates to the kinetic energy of the turbulent flow and $\epsilon$ determines the scale of the turbulence. $\epsilon$ also takes into account the fluctuating vorticity of the flow. The stress components $\overline{u'^2}$, $\overline{v'^2}$ and $\overline{w'^2}$ are assumed equal. The method solves the Navier-Stokes equations in 3D environment but gives them an approximate time-averaged solution. Thus, the fluid flow solution is a rejection of all exact parameters replaced by time-averaged ones instead. [33, 34]

### 3.4.2 Contact Modelling and Connections

The contact and joint modelling consists of two main techniques: inclusion of flexible bushing joints to decouple the above-mentioned subsystems and standard ANSYS contacts. Flexible joints are analytically defined as stiffness matrices, which describe the behaviour of the bellows (see annex *E*). [35] All standard contacts were considered as bonded contacts. Adjacent surfaces of stiffness matrices were thermally coupled.

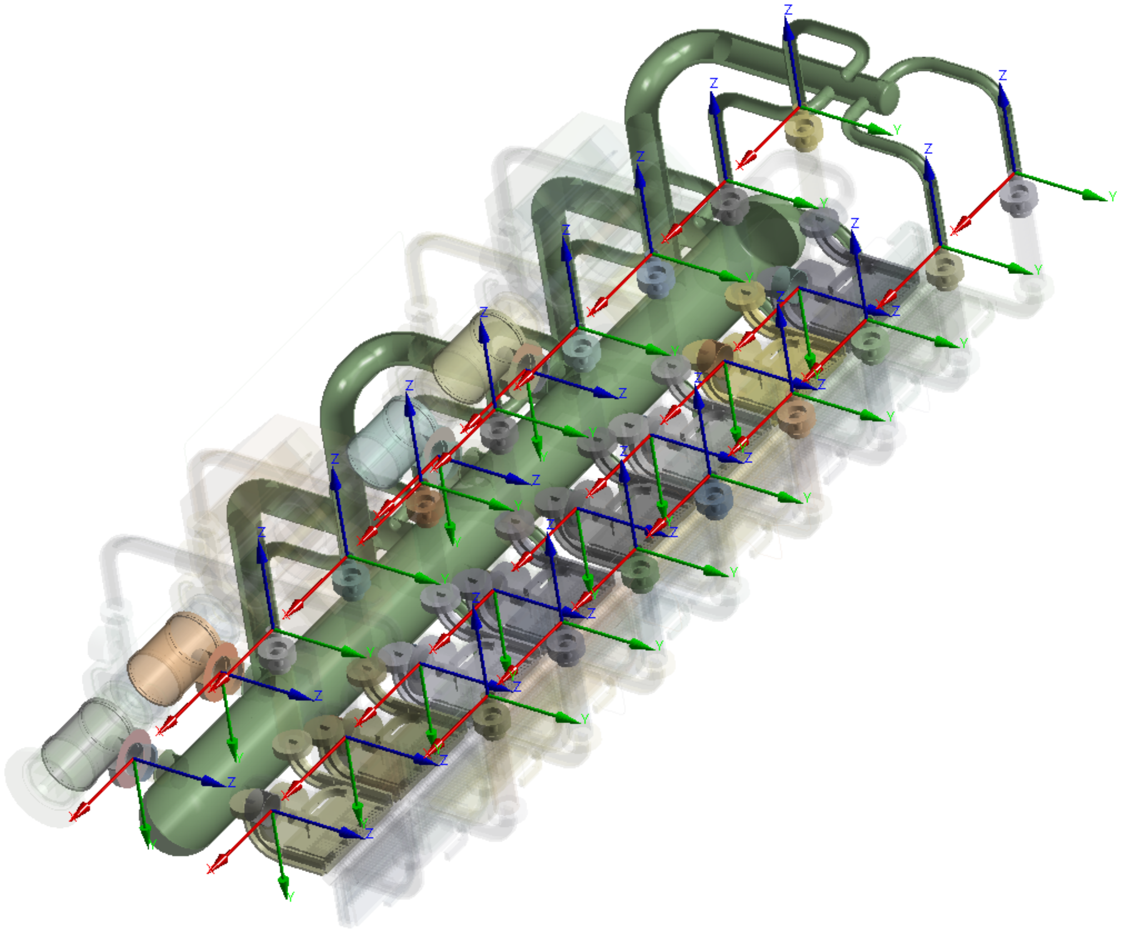

Figure 3.10: Illustration of the contact modelling for the vacuum interconnections.

All contact modelling has been optimized for the lightest possible computation because of the large number of contacts and joints in the model. Illustration of contact modelling and joints is shown in figure 3.10. Although several different contact types were considered, the so-called bonded contact turned out to be the most feasible for TMM. In bonded contact the common areas share all the d.o.f.s. Other kinds of contacts such as frictional, frictionless or separate would result into a nonlinear contact model. Even in frictionless contact modelling the contact surfaces around the contact area are not constant due to deformation and thus, several sub steps are required during the solution phase. Both MB and DB RF structures are constrained using both fixed and sliding supports. This allows the AS to expand freely along its length during the different operation modes.

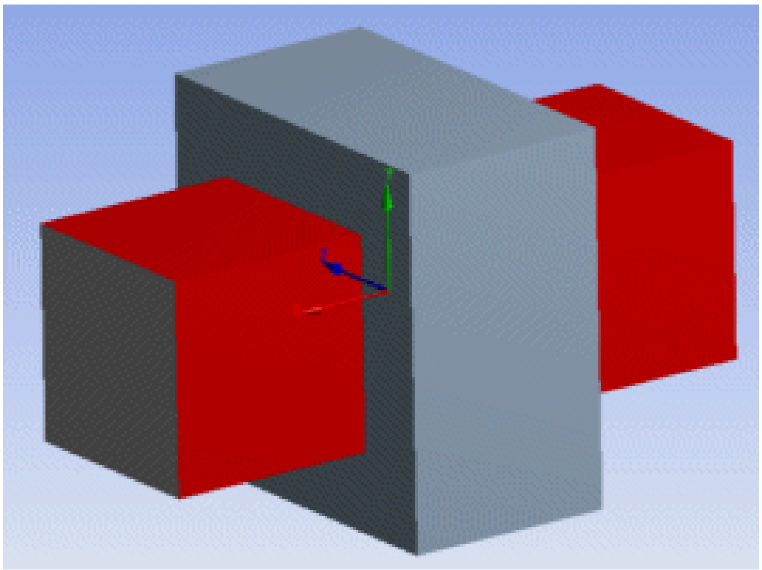

Figure 3.11: The sliding effect can be taken into account via so-called Ansys translational joint, which allows the contacting surfaces to slide in one translational direction and fixing all the others.

In the current TMM the structural FEA was improved by taking into account the more realistic boundary conditions regarding the contact areas between the RF components and V-shape supports. The sliding effect was taken into account using a translational joint contact locking all other degrees of freedom besides longitudinal movement. [37, 36] Using this approach notifying the more realistic contact between the RF structures compared to bonded one, a sliding condition can be taken into account in TMM. Moreover, the method does not iterate the contact area during solution, which will ease the computation significantly and does not lead into convergence problems. The contact also allows parameters for frictional analysis.

### 3.4.3 Supports

The CLIC RF structures are currently supported on V-shaped precision supports, which are mounted on the MB and DB girders. The girders are attached to so-called cradles, which serve as articulation points for adjacent girders. The cradles are supported on movers made of adjustable high precision linear actuators. The girder end supports are divided into master and slave cradles enabling a coupled support of adjacent girders. The above-mentioned coupling is so called "snake" concept, which allows the alignment of the long linear accelerator as a whole. The modelled supporting system idealization is shown in figure 3.12.

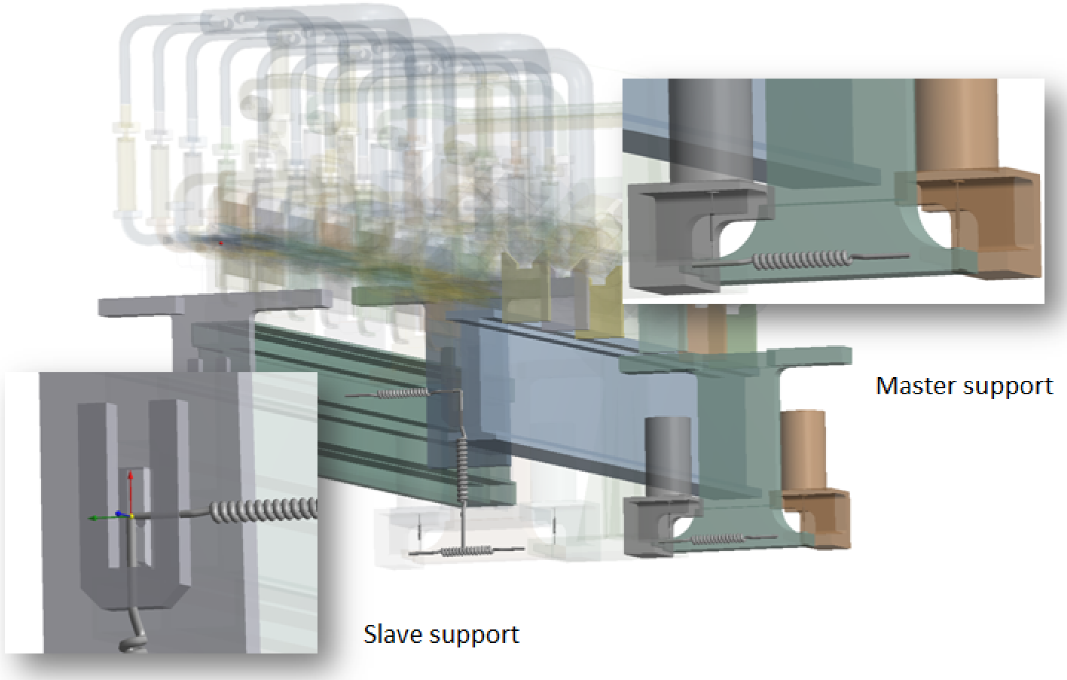

Figure 3.12: The CLIC module is supported on the kinematic stands, constructed of a high precision linear actuators. Master support (right) and slave support (left).

The ANSYS modelling was done to the level of the mounting surface of the lower ends of the actuator. As a result, the estimated stiffness of the actuator support was taken into account. The actuator support containing six d.o.f. constraints was reduced to equally stiff linear and torsion springs to ease the computation. Both the master and slave cradle end designs were introduced into the model.

## 3.5 Meshing Controls

### 3.5.1 Solving a Large-Scale Multi-Physics Model

For a such complex model as presented in this thesis, the computation is time consuming and especially the structural FEA requires explicit manual controlling. The model presented includes meshing optimization on each part. The overall mesh is shown in figure 3.13

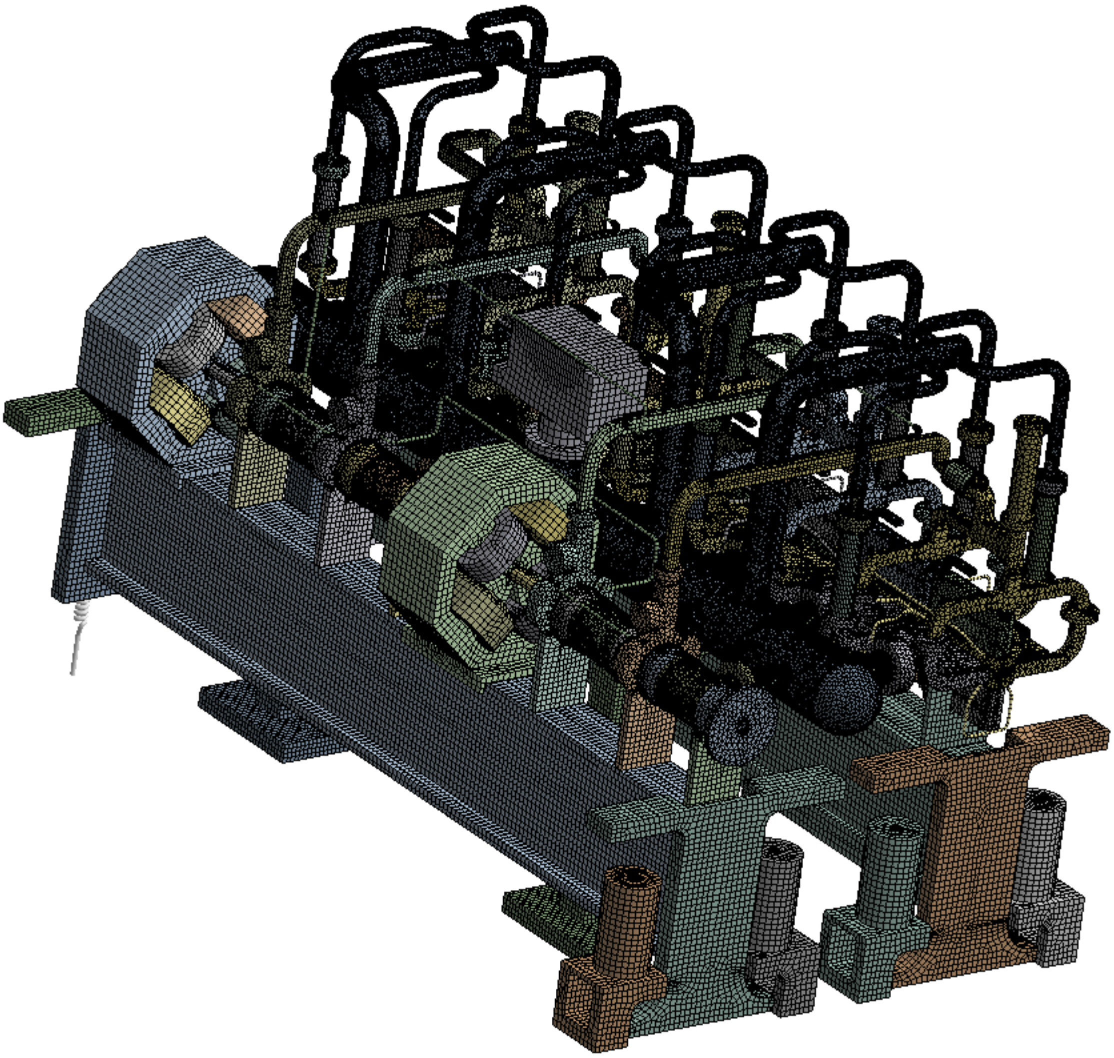

Figure 3.13: Illustration of the generated overall mesh for the CLIC two-beam module.

The meshing control highlights are presented as follows:

- sweep was used where possible;
- element sizing on each module componenet;
- tetrahedral meshing and hexahedral meshing where possible;
- both linear and quadratic elements were introduced;
- the main element for thin walled parts is SOLSH90;
- for surfaces having thermal coupling SURF152 elements were used;
- for coupling 1D fluid-thermal elemens into a 3D thermal elements, a FLUID116 element was used;

In figure 3.14 the meshing is shown for the WG sub-assembly including sweep and hexahedral meshing.

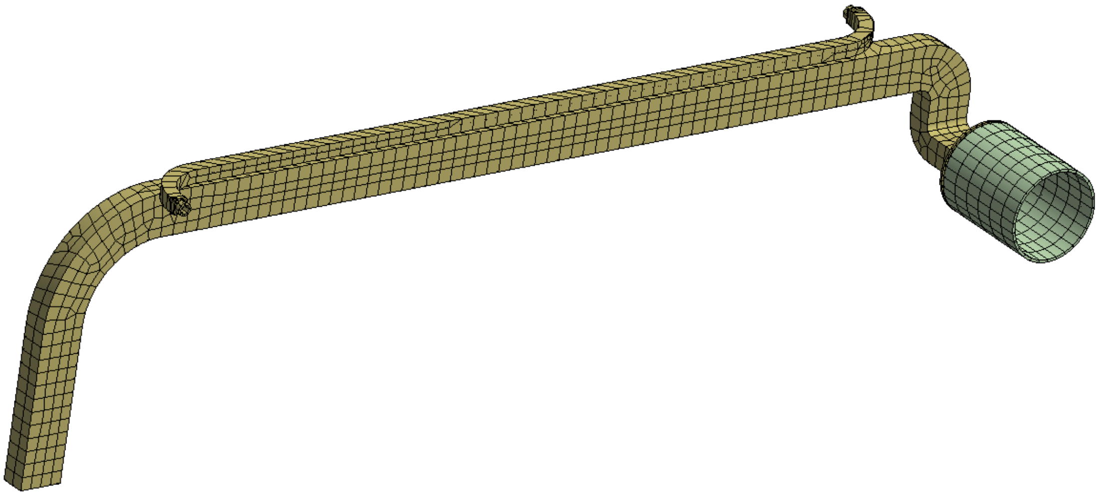

Figure 3.14: For the simple module sub-assemblies such as the WG, a sweep method with hexahedral meshing can be applied rather easily yielding more accurate results and numerically lighter modelling.

Several sub-components were successfully meshed using hexahedral options, which usually reduce the overall amount of elements used on the component and still yield in more accurate results over tetrahedral ones. The meshing routines in commercial FEA softwares, such as ANSYS, using of tetrahedral elements have become quite robust. Although there are meshing routines for volumes using brick elements, they are not as robust and may not always work for complex volumes. This problem was encountered also in the TMM. Nevertheless, for the thin profiles, the thickness has to studied more carefully and layers should be adjusted accordingly. In figure 3.15 a typical cylinder tube used in TMM is shown including layer adjustment. Within the layer nodes, the displacement is linearly interpolated

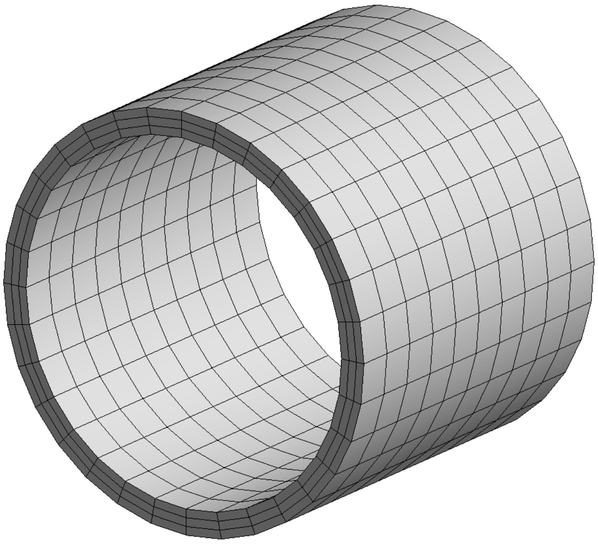

Figure 3.15: Illustration of layer adjustment.

For this reason the tetrahedral elements are useful. However, the problem is that traditionally tetrahedral elements used as finite elements are not as well behaved as brick elements. Hence, one has to be careful with tetrahedral elements.

In general it can be said that linear tetrahedral elements perform poorly in problems with plasticity, nearly incompressible materials and acute bending. Often the so-called locking problems associated with nonlinear modelling cases have forced analysts to employ hexahedral formulations. For a variety of reasons, low-order tetrahedral elements are preferable to quadratic tetrahedral elements. [38]

The meshing included about 5 million nodes resulting in the degrees of freedom in the model of tens of millions. Moreover, a model of this complex requires a computing power and memory beyond the standard desktop PCs. Therefore, the model was solved by using a separate virtual computing unit available, which still uses Windows environment. For parallel computing, a Linux batch run solver was recommended. However, a model constructed originally in a Windows environment usually counters difficulties in convergence when using a Linux batch. This results into stability problems between operation systems and thus, the model was solved using its original OS. The overall solution time was tens of hours including multiple solution phases with different load steps.

# 4. RESULTS

Based on the module input data, a set of thermal and structural results were obtained. In figure 4.1 the water flow temperature distribution is shown inside the cooling channels in unloaded operation. The temperature rise is about 10°C.

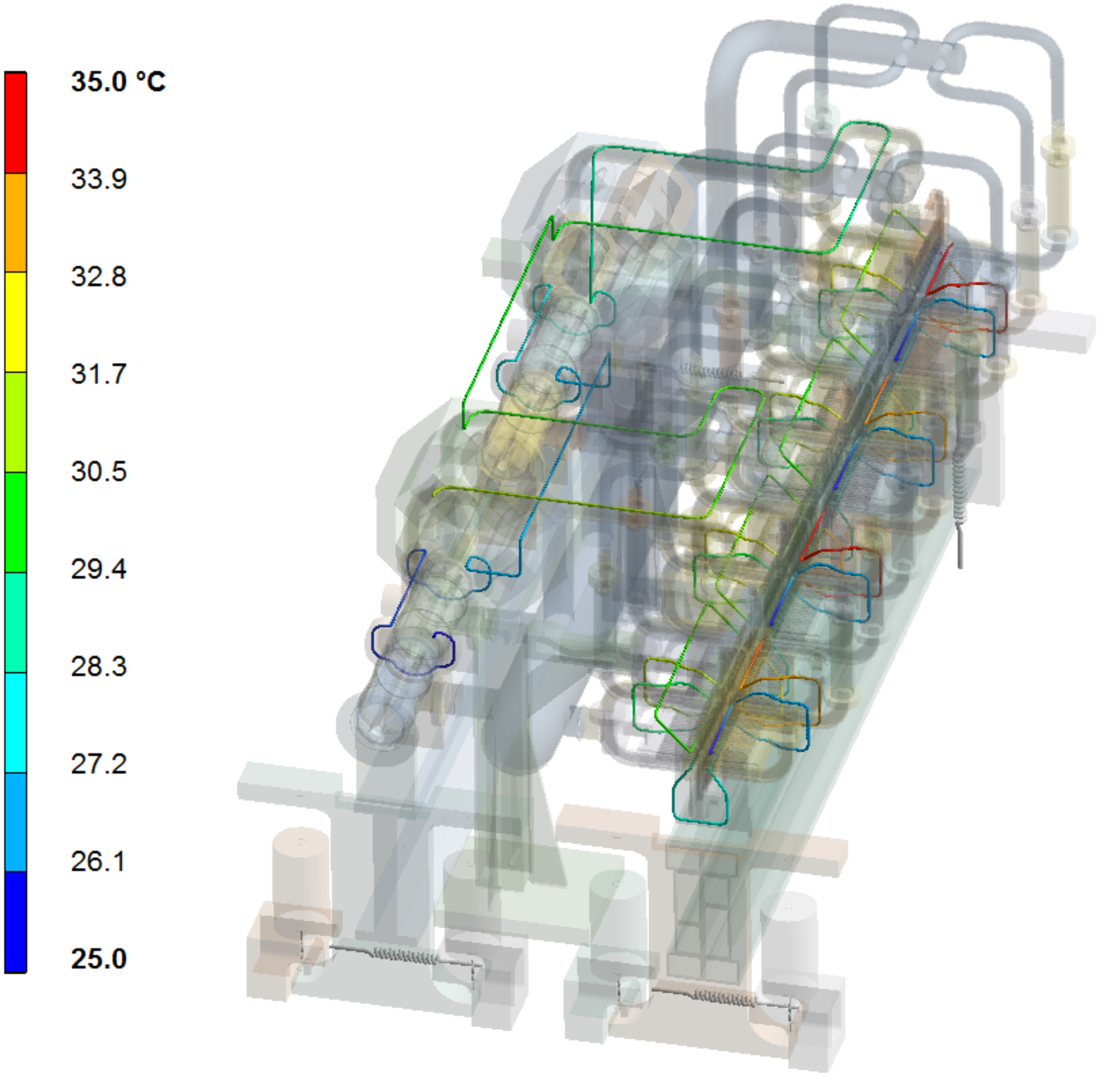

Figure 4.1: Water temperature distribution inside the cooling channels in unloaded operation mode.

In figure 4.2 the temperature distribution on module is presented when the thermal loading is ramped up to unloaded operation mode. The temperature on the outer surfaces exceeds 40° C. In annex F.1 the temperature contours for the SAS is presented, which undergoes the most significant temperature rise.

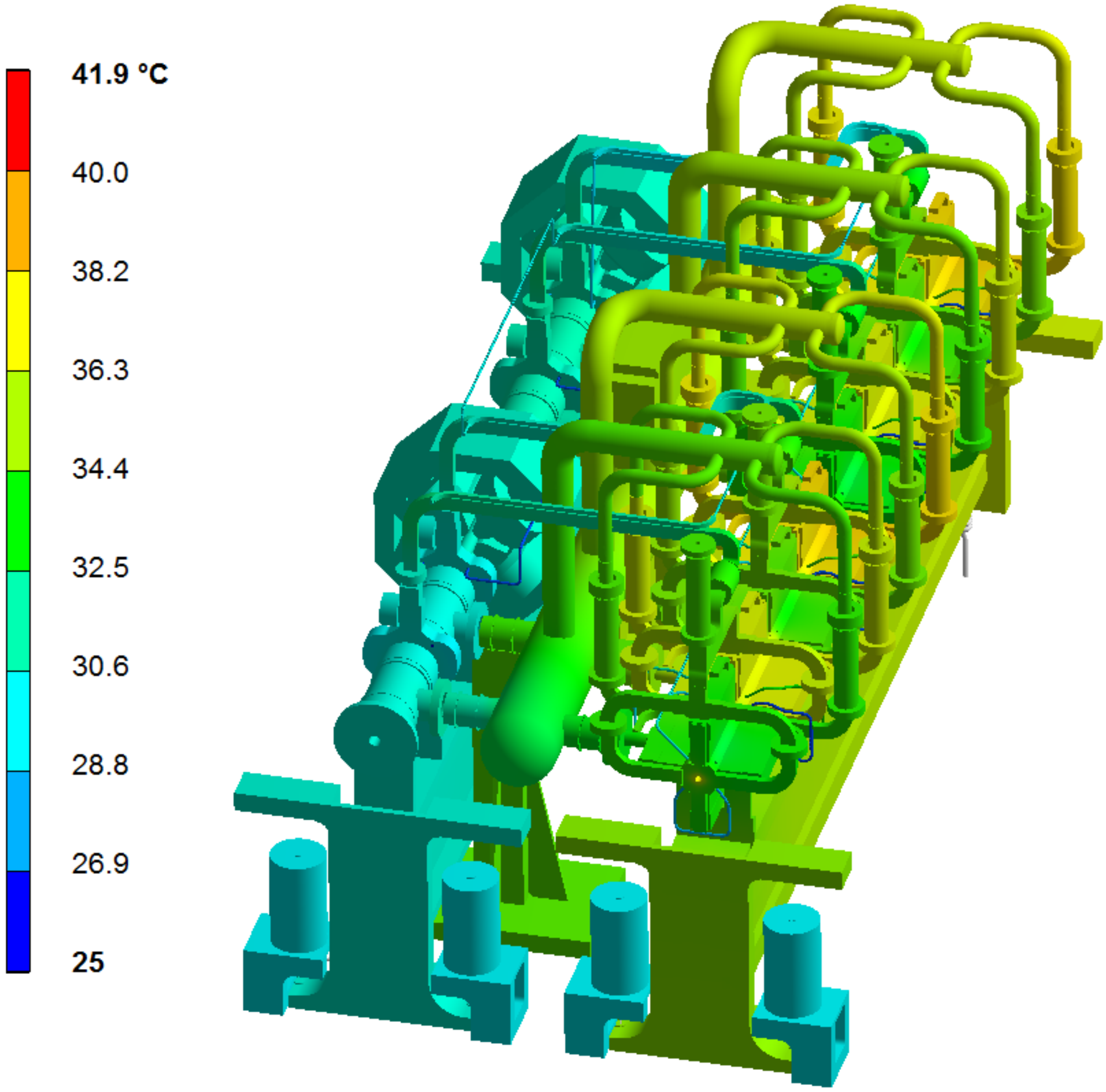

Figure 4.2: Temperature distribution along the module corresponding the unloaded operation mode.

In figure 4.3 the temperature distribution on module is presented when the operation of the module is changed to loaded case. The temperature on the outer surfaces are about 40° C.

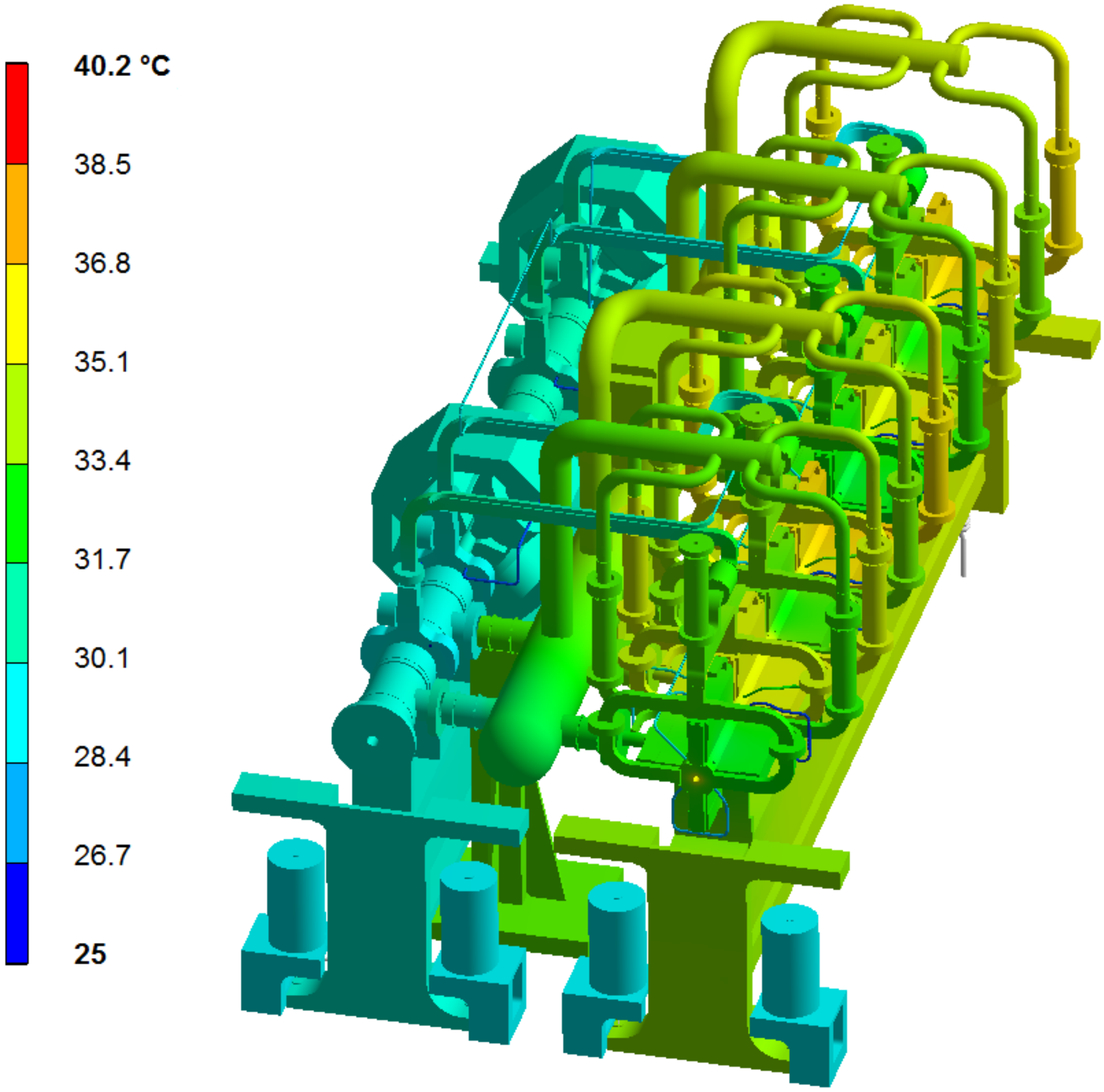

Figure 4.3: Temperature distribution along the module corresponding the loaded operation mode.

After obtaining the thermal response of the module, the results were imported into ANSYS structural environment. The gravity, vacuum and RF loads were calculated in steps. Figure 4.4 shows the deformation contours for the module based on the thermal inputs in unloaded operation. In annex H.1 the longitudinal deformation for the SAS in shown.

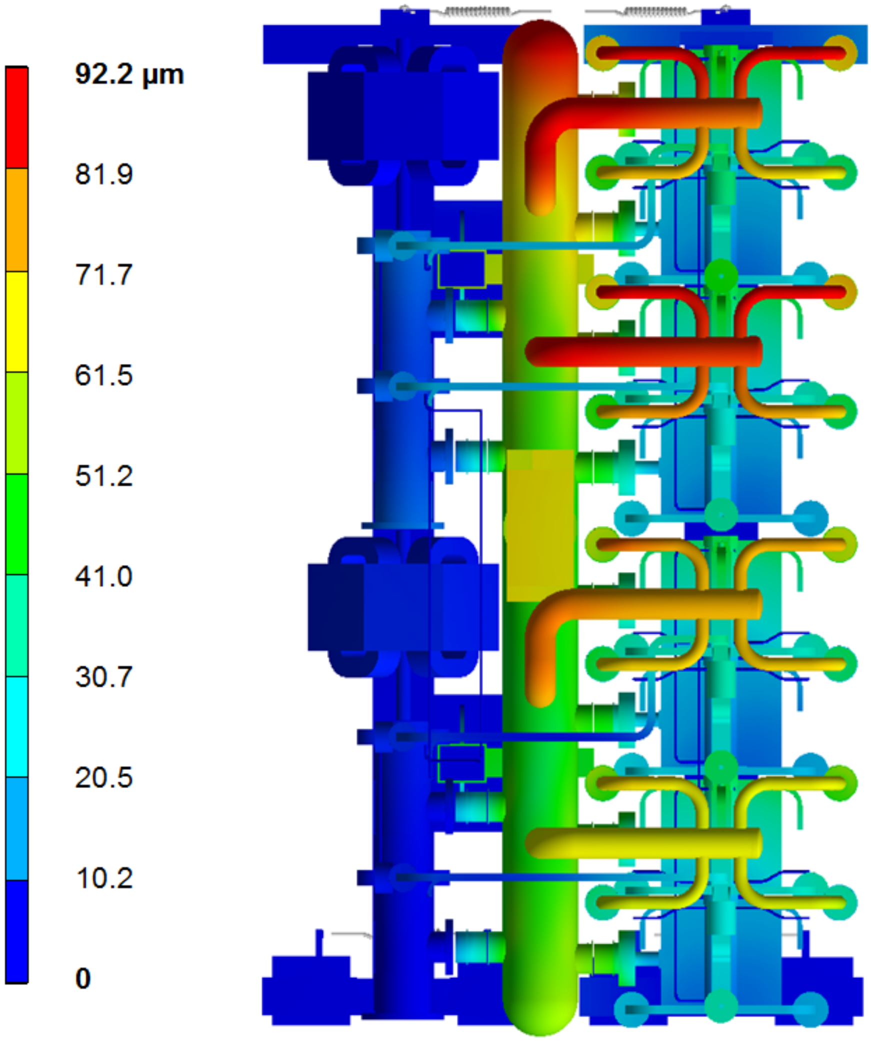

Figure 4.4: Deformation contour for the module in case only the RF load is applied.

In figure 4.5 the deformation contours for the module is presented when the vacuum load is applied. The deformation under gravity is seen in annex G.1.

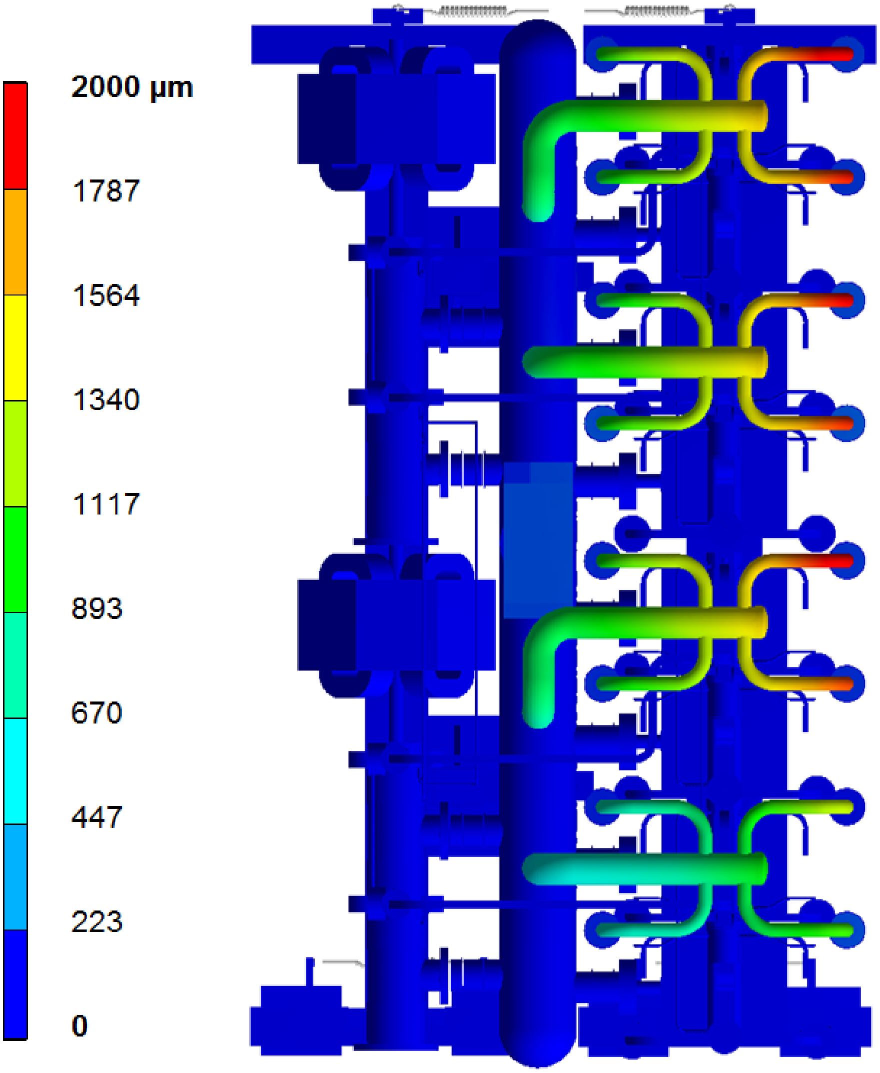

Figure 4.5: Deformation contour for the module when the vacuum load is applied.

The highest stresses are seen on AS iris surface, where the temperature has its largest variance causing thermal stresses. The stresses are shown in figure 4.6. The maximum stress observed was about 9 MPa.

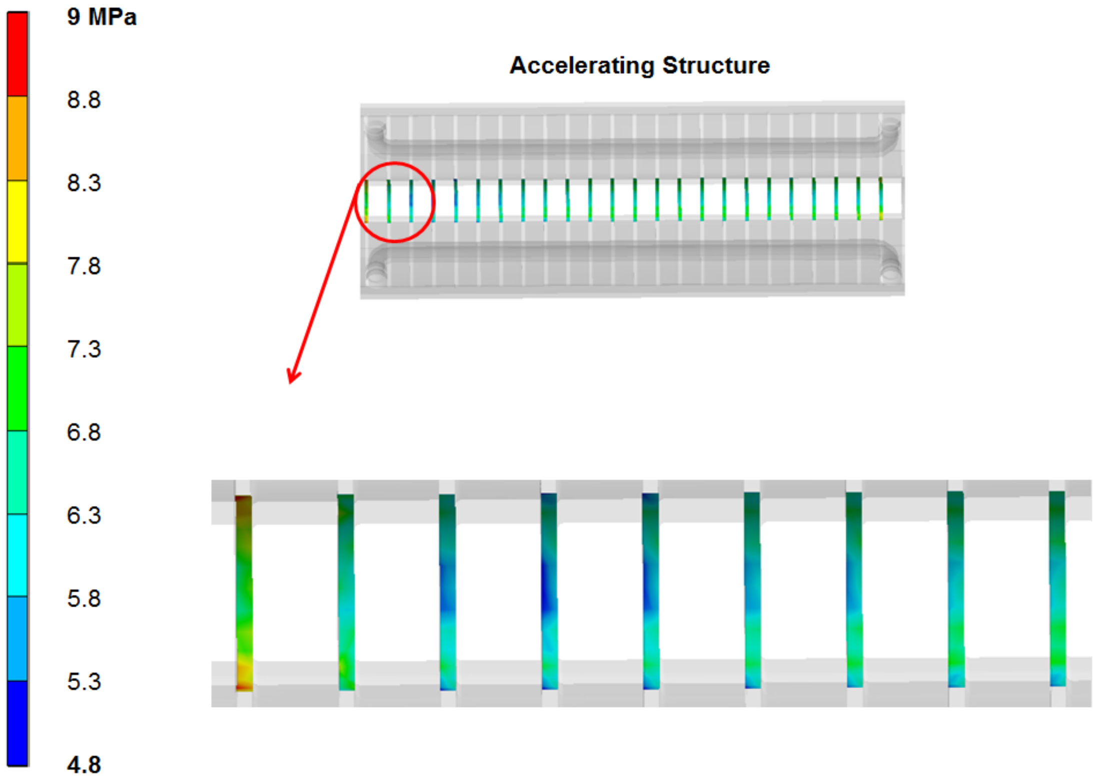

Figure 4.6: Stresses at the AS iris surface.

The obtained thermal results are summarized in table 4.1. The transferred heat into the air can be approximated from the equation 3.7 since the absorbed heat into the water is known.

Table 4.1: Summary of the thermal results obtained for the module.

| Item | Unloaded | Loaded |
|---|---|---|
| Max. temp. of the module | 41.9 ° C | 40.2 ° C |
| Water output temperature MB | 35.0 ° C | 34.92 ° C |
| Water output temperature DB | 29.8 ° C | 29.8 ° C |
| Heat to water / air | 3384/100 W | 2797/91.0 W |

In table 4.2 the structural results are shown for unloaded and loaded operation modes, respectively. Note that only the RF power on AS is varied between the modes.

Table 4.2: Summary of the structural results; G: gravity, V: vacuum, RF: thermal load.

| Item | Unloaded | Loaded |
|---|---|---|
| Max. def at MB line (G) | 30 $\mu$m | 30 $\mu$m |
| Max. def at DB line (G) | 35 $\mu$m | 35 $\mu$m |
| Max. def at MB line (V) | 49 $\mu$m | 49 $\mu$m |
| Max. def at DB line (V) | 10 $\mu$m | 10 $\mu$m |
| Max. def at MB line (RF) | 40 $\mu$m | 36 $\mu$m |
| Max. def at DB line (RF) | 13 $\mu$m | 13 $\mu$m |

# 5. DISCUSSION

The thermal results show that following the RF power dissipation, the temperature of the module rises over 10°C. The most significant temperature rise is seen on the AS and especially at the end of each AS. The current cooling system does not create a symmetrical temperature gradient on the AS sections, and as a result the AS irises does not have the same temperature around the perimeter. Eventually this will lead into non-symmetric mechanical response of the MB. The phenomena could be still improved by using different cooling design. Yet, according to the results, the deformation between two operation modes varies only by few micrometers. Between different operation modes, the dilation due to temperature variation is smaller and could be adjusted by the coolant mass flow. In the current model, the thermal dissipation to air was about 50W/m of a total heat dissipation of 1.7kW/m. At the moment, the total limit for the dissipation to air is set to 150W/m, which is mainly governed by the size of the tunnel ventilation system.

According to the results the most significant mechanical distortion origins from the thermal dissipation, which cause the structure to expand mainly in longitudinal direction. Although, when comparing the obtained results to the ones calculated for simplified module configuration and the so-called CLIC two-beam module to be tested in the laboratory without the beam [39, 40], where the AS-AS interconnection was considered as fixed, the longitudinal deformation is seen significantly smaller. Moreover, the previous models assumed fixed contacts between the module components, namely the interconnection between RF structures and the V-shape supports. The current model introduced also the sliding effects, which were neglected in the past. In TMM the deformation due to gravity is directly interlinked to the actuators supporting MB and DB. Thus, the deformation values presents the overall drop of the module under gravity load. The actual deformation of the RF structures under gravity has to be considered significantly smaller. During the operation the effect of gravity is naturally compensated by construction.

The forces created by the vacuum cause mainly transverse deformation to the module. In the current module configuration the vacuum connections into the AS and PETS has not only horizontal but also vertical orientation, which compensates partly to each other. In the case, where the vacuum connection into the MB and DB side has only horizontal orientation, the vacuum based deformation is seen larger

[39]. Since the vertical vacuum connection will not prevent the horizontal deformation completely, more stable vacuum response could be achieved, if the horizontal force created by the vacuum interconnection is compensated with an equivalent one from the adjacent side of the vacuum reservoir and the MB/DB side. This kind of behavior could be achieved by using different pumping technology. [41] It has been suggested that the current vacuum reservoir could also be replaced by so-called minipumps. The minipumps would be connected to each AS and PETS separately in order to create the needed vacuum environment. In general, the minipumps would offer light, compact and large pumping speed for the module.

In general the stresses seen on the CLIC two-beam module are very small since various flexible interconnections are used. Therefore, no significant stresses are seen. However, since the dissipated RF power causes the maximum temperature rise on the AS iris surface, the observed thermal von-Mises stress of about 9 MPa could have an influence on structural fatigue and damage during the planned CLIC lifetime. It should be noted that the fatigue of a material occurs already below the material yield strength. Thus, future study especially on the material based research for the AS would be beneficial.

# 6. CONCLUSION

A FEM model has been presented, which corresponds to the current complexity of the CLIC two-beam module layout, enabling an overall assessment of the thermo-mechanical response. According to the results, the interpretation of the stability of CLIC RF structures at micron level is viable. Although, as notified in the modelling phase, the adjustments made for the meshing controls and especially for the contacts has a major role in assessment of the mechanical behavior of the current complex. The future aim in TMM should focus on achieving a more efficient model in computational point of view. By optimizing the meshing methodology presented here even further, the future configurations could be solved in less time which would provide better control on the structural FEA. Inclusion of shell elements replacing the current hexahedral elements especially on the vacuum manifold area can be considered as a such improvement. Also the utilization of beam elements for the MB and DB girders should be considered. Therefore, the TMM could still be improved in future configurations and the accuracy of the model can be improved further. Also the planned two-beam module tests in the future are expected to give better understanding of the module behavior under applied thermal and mechanical loading showing the critical points still to be improved, which can be propagated back to the current simulation model. Apart from the thermal response of the module, whose accuracy is better known, the final structural behavior of the TMM can be justified best with comparative test results. Even though increased computational power used in the field of numerical analysis nowadays, the powerful finite element method alone can be still considered as a poor guide but a good accomplisher towards better engineering approaches.

Using the presented modelling principles in this thesis as baseline, the TMM can be carried out for other types of CLIC modules in the future by modifying the current configuration accordingly. Also the possible improvements pointed out should be considered. As pointed out for the most critical components, a 3D CFD could be considered in order to validate the mechanical response of the structure under fluid flow caused effects. The influence of the minipumps on the modules structural behavior could be analysed more closely in future and thus, comparison could be made according to the simulation results concerning the possible differences in order to aid the design group towards better solutions.

# REFERENCES

[1] J. R. Ellis. Physics Goals of the Next Century at CERN, AIP Conf. Proc., vol. 542, no. hep-ph/0002117. CERN-TH-2000-050, pp. 267-292. 23 p, Feb 2000.

[2] CERN (2008): CERN in a Nutshell. 26.09.2011. [Online] Available at: http://public.web.cern.ch/public/en/About/About-en.html.

[3] CERN (2008): A Global Endeavour. 26.09.2011. [Online] Available at: http://public.web.cern.ch/public/en/About/Global-en.html.

[4] CERN (2008): Physics for Health. 26.09.2011. [Online] Available at: http://public.web.cern.ch/public/en/About/BasicScience9-en.html.

[5] Ellis, J R. Wilson, I. New Physics with the Compact Linear Collider, CLIC-Note-466, CERN (2000).

[6] G. Geschonke. The Next Energy-Frontier Accelerator a Linear e+ e- Collider?. CERN-OPEN-2010-007. CLIC-Note-807.

[7] CERN Courier (2008): CLIC Here for the Future. 26.09.2011. [Online] Available at: http://clic-study.web.cern.ch/CLIC-Study/Publications/CCSepCLIC_final.pdf.

[8] J.P.Delahaye: Towards CLIC Feasibility, IPAC'10, FRXCMH01, Kyoto, Japan, 23-28 May 2010.

[9] Braun, H. Corsini, R. Delahaye, J P. de Roeck, A. Döbert, S. Ferrari, A. Geschonke, Günther. Grudiev, A. Hauviller, Claude. Jeanneret, B. Jensen, E. Lefèvre, T. Papaphilippou, Y. Riddone, G. Rinolfi, L. Schlatter, W D. Schmickler, Hermann. Schulte, D. Syratchev, I. Taborelli, M. Tecker, F. Tomás, R. Weisz, S. Wuensch, W. CLIC Parameters 2008. CERN-OPEN-2008-021; CLIC-Note-764.2008.

[10] Riddone, G. Schulte, D. Mainaud-Durand, H. Syratchev, I. Wuensch, W. Zennaro, R. Nousiainen, R. Samoshkin, A . Technical Specification for the CLIC TwoBeam Module, 11th European Particle Accelerator Conference, Genoa, Italy, 2008.

[11] Soldatov, V. Samoshkin, A. Gudkov, D. Atieh, S. Grudiev, A. Khan, V F. Riddone, G. D?Elia, A. Jones, RM. Engineering Design and Fabrication of X-Band Damped Detuned Structure for the CLIC Study. CERN-ATS-2011-046. 2011.

[12] R. Ruber. CLIC Feasibility Demonstration at CTF3. MO303. LINAC'10. Kyoto, Japan.

[13] Mirapeix, F. Castillo, J. Ortiz, A. Añel, J. Urzainki, A. Aldalur, X. Amores, J. Status of the Manufacturing of Accelerating Structures for LINACS. TUPC010. Proceedings of IPAC2011, San Sebastián, Spain. 2011

[14] Wuensch, W. CLIC Accelerating Structure Development, EPAC'08, Italy, THXM01 (2008).

[15] Heikkinen, S. Thermally Induced Ultra High Cycle Fatigue of Copper Alloys of the High Gradient Accelerating Structures. CERN-THESIS-2010-218. CLIC-Note-859. (2010)

[16] Nousiainen, R. Accelerating Structure Cooling Parameter Specification. EDMS No: 964717 v.1. 2008.

[17] Nousiainen, R. Syratchev, I. PETS Cooling Parameter Specification. EDMS No: 964715 v.2. 2008.

[18] TE Department / CLIC Project. Technical Specification for the Drive Beam Quadrupole Magnets for the CLIC Test Facility. EDMS No: 1135434. 2011.

[19] Gudkov, D. Riddone, R. Samoshkin, A. Solodko, A. Two-Beam Module. 2011. 30.09.2011. [Online] Available at: http://project-clic-cdr.web.cern.ch/project-CLIC-CDR/Drafts/TwoBeamModule.pdf.

[20] I.Syratchev. Present On/Off Scheme with a Choke Based Tunable Reflector. EDMS node 1033084 v.1.

[21] R. Nousiainen. Design Specification for Supporting and Alignment Systems of a Linear Particle Collider. CERN-THESIS-2010-033. CLIC-Note-778. 2008.

[22] D. Schulte. Beam-Based Alignment in the New CLIC Main LINAC. CERN-ATS-2009-136. CLIC-Note-804. (2009)

[23] Gazis, N. Riddone, G. Griffet, S. Samoshkin, A. Fabrication and Validation of the Prototype Supporting System for the CLIC Two-Beam Modules. TUPC012. Proceedings of IPAC2011, San Sebastián, Spain. 2011.

[24] Gazis, N. Riddone, R. Mainaud-Durand, H. Samochkine, A. Anastasopoulos, M. Study and Application of Micrometric Alignment on the Prototype Girders of the CLIC Two-Beam Module. CERN-OPEN-2011-020. CLIC-Note-878. (2011)

[25] Raatikainen, R. Nousiainen, R. Österberg, K. Riddone, G. Samoshkin, A. Gudkov, D. Applying One-Dimensional Fluid-Thermal Elements into a 3D CLIC Accelerating Structure. CERN-OPEN-2011-032. CLIC - Note - 881.

[26] Workbench-Simulation Heat Transfer 11.0. Workshop 10: Fluid Thermal Elements and Thermal Stress Analysis. [ANSYS reference]

[27] Ansys Workbench/Classic 12.1 Tutorial, FLUID116. [Element reference]

[28] T. J. Chung. Computational Fluid Dynamics. Cambridge. Second Edition. 2010. 1034 p. ISBN: 978-0-521-76969-3.

[29] Welty, J. Wicks, C E. Rorrer, G L. Wilson, R E. Fundamentals of Momentum Heat, and Mass Transfer. New York. John Wiley & Sons. Fifth Edition. 711 p. ISBN-13 978-0470128688.

[30] Zienkiewicz, O C. Taylor, R L. Nithiarasu, P. The Finite Element Method for Fluid Dynamics. Oxford. Butterworth-Heinemann. 2005. 435 p. ISBN 0 7506 6322 7.

[31] Tessa, C. Ryan, K. Boland, M. Riddone, G. Samoshkin, A. Flow Induced Vibrations of the CLIC X-band Accelerating Structures. MOPC002. Proceedings of IPAC'11, San Sebastian, Spain. 2011.

[32] Durbin, P A. Pettersson-Reif, B A. Statistical Theory and Modeling for Turbulent Flow. John Wiley & Sons. Second Edition. 2010. 372 p. ISBN-978-0-470-68931-8.

[33] Bardina, J.E. Huang, P G. Coakley, T.J. Turbulence Modeling Validation, Testing, and Development, NASA Technical Memorandum 110446. 1997.

[34] Munson, R. Young, D F. Okiishi, T H. Fundamentals of Fluid Mechanics. New York. John Wiley & Sons. Fourth Edition. 2002. 856 p. ISBN: 0-471-44250-X.

[35] BOA Metal Bellows Consultant. Edition 20.0-UK. [BOA HANDBOOK]

[36] Translational joint contact. [ANSYS MANUAL]

[37] M. Xie. Flexible Multibody System Dynamics: Theory and Applications. Washington. Taylor & Francis. 1994. 214 p. ISBN 1-56032-300-0.

[38] Puso, M. Solberg, J. A Stabilized Nodally Integrated Tetrahedral. Int. J. Numer. Meth. Engng 2006; Vol. 67:841-867. 6 August 2006.

[39] Nousiainen, R. Österberg, K. Riddone, G. Studies on the Thermo-Mechanical Behavior of the CLIC Two-Beam Module. Proceedings of Linear Accelerator Conference LINAC2010, Tsukuba, Japan. 2010.

[40] Raatikainen, R. Niinikoski, T. Österberg, K. Riddone, G. Progress on Modeling of the Thermo-Mechanical Behavior of the CLIC Two-Beam Module. TUPC018. Proceedings of IPAC'11, San Sebastian, Spain. 2011.

[41] SAES-GETTERS. NEXTorr Brochure. 2010. 04.10.2011. [Online] Available at: http://www.saesgetters.com/documents/NEXTorr%20Brochure%202010_1842 .pdf

# APPENDIX

A. CLIC Two-Beam Module CATIA 3D Illustration

B. Schematic of the CLIC Two-Beam module layout

C. Fluid-Thermal (APDL) Command Snippet

D. SAS Heat Flux (APDL) Command Snippet

E. ANSYS Bushing Joint Definition Matrices

F. Temperature contours for the SAS under RF load

G. Deformation contours for the module under gravity load

H. Deformation contours for the SAS under RF load

# A. CLIC TWO-BEAM MODULE CATIA 3D ILLUSTRATION

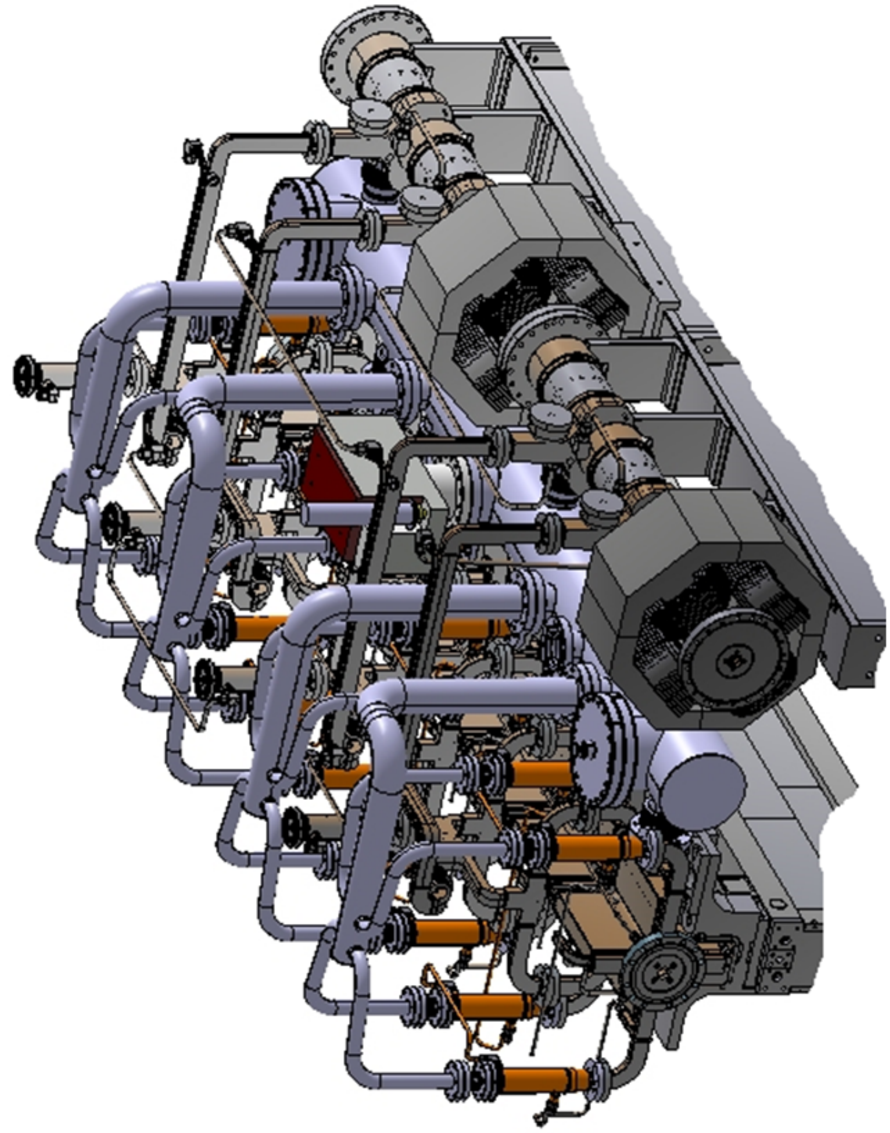

Figure A.1: CLIC two-beam standard module CATIA 3D illustration.

# B. SCHEMATIC OF THE CLIC TWO-BEAM MODULE LAYOUT

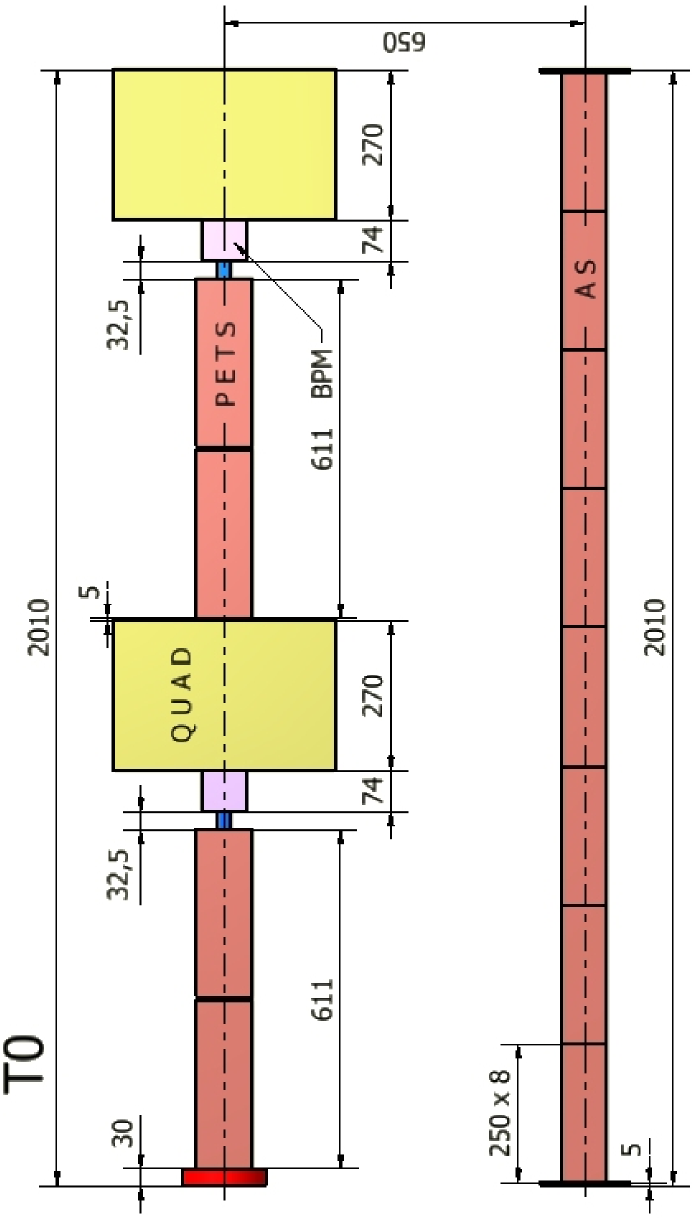

Figure B.1: Schematic of the CLIC Two-Beam module layout (units in millimeters).

# C. SAS HEAT FLUX (APDL) COMMAND SNIPPET

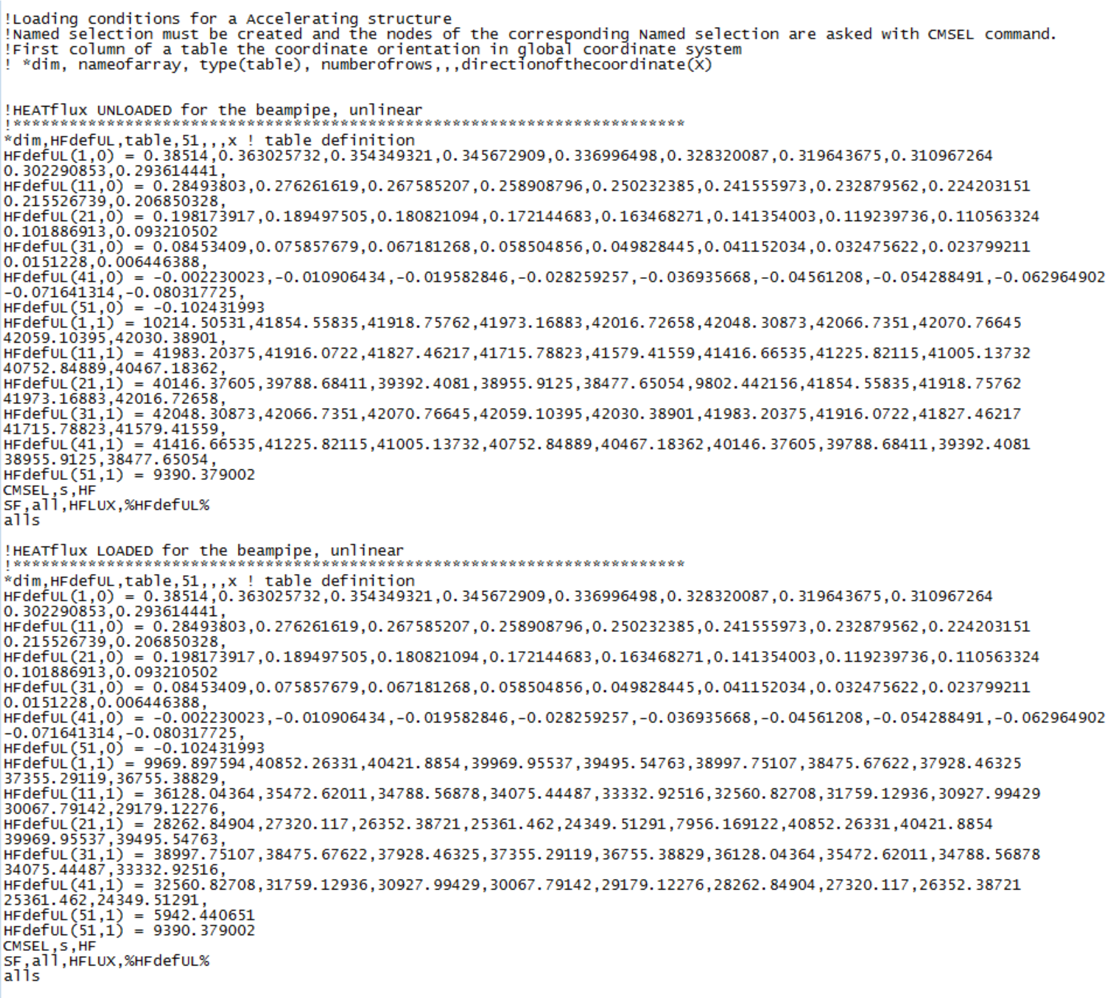

```
!Loading conditions for a Accelerating structure
!Named selection must be created and the nodes of the corresponding Named selection are asked with CMSEL command.
!First column of a table the coordinate orientation in global coordinate system
! *dim, nameofarray, type(table), numberofrows,,,directionofthecoordinate(X)


!HEATflux UNLOADED for the beampipe, unlinear
!************************************************************************
*dim,HFdefUL,table,51,,,x ! table definition
HFdefUL(1,0) = 0.38514,0.363025732,0.354349321,0.345672909,0.336996498,0.328320087,0.319643675,0.310967264
0.302290853,0.293614441,
HFdefUL(11,0) = 0.28493803,0.276261619,0.267585207,0.258908796,0.250232385,0.241555973,0.232879562,0.224203151
0.215526739,0.206850328,
HFdefUL(21,0) = 0.198173917,0.189497505,0.180821094,0.172144683,0.163468271,0.141354003,0.119239736,0.110563324
0.101886913,0.093210502
HFdefUL(31,0) = 0.08453409,0.075857679,0.067181268,0.058504856,0.049828445,0.041152034,0.032475622,0.023799211
0.0151228,0.006446388,
HFdefUL(41,0) = -0.002230023,-0.010906434,-0.019582846,-0.028259257,-0.036935668,-0.04561208,-0.054288491,-0.062964902
-0.071641314,-0.080317725,
HFdefUL(51,0) = -0.102431993
HFdefUL(1,1) = 10214.50531,41854.55835,41918.75762,41973.16883,42016.72658,42048.30873,42066.7351,42070.76645
42059.10395,42030.38901,
HFdefUL(11,1) = 41983.20375,41916.0722,41827.46217,41715.78823,41579.41559,41416.66535,41225.82115,41005.13732
40752.84889,40467.18362,
HFdefUL(21,1) = 40146.37605,39788.68411,39392.4081,38955.9125,38477.65054,9802.442156,41854.55835,41918.75762
41973.16883,42016.72658,
HFdefUL(31,1) = 42048.30873,42066.7351,42070.76645,42059.10395,42030.38901,41983.20375,41916.0722,41827.46217
41715.78823,41579.41559,
HFdefUL(41,1) = 41416.66535,41225.82115,41005.13732,40752.84889,40467.18362,40146.37605,39788.68411,39392.4081
38955.9125,38477.65054,
HFdefUL(51,1) = 9390.379002
CMSEL,s,HF
SF,all,HFLUX,%HFdefUL%
alls

!HEATflux LOADED for the beampipe, unlinear
!************************************************************************
*dim,HFdefUL,table,51,,,x ! table definition
HFdefUL(1,0) = 0.38514,0.363025732,0.354349321,0.345672909,0.336996498,0.328320087,0.319643675,0.310967264
0.302290853,0.293614441,
HFdefUL(11,0) = 0.28493803,0.276261619,0.267585207,0.258908796,0.250232385,0.241555973,0.232879562,0.224203151
0.215526739,0.206850328,
HFdefUL(21,0) = 0.198173917,0.189497505,0.180821094,0.172144683,0.163468271,0.141354003,0.119239736,0.110563324
0.101886913,0.093210502
HFdefUL(31,0) = 0.08453409,0.075857679,0.067181268,0.058504856,0.049828445,0.041152034,0.032475622,0.023799211
0.0151228,0.006446388,
HFdefUL(41,0) = -0.002230023,-0.010906434,-0.019582846,-0.028259257,-0.036935668,-0.04561208,-0.054288491,-0.062964902
-0.071641314,-0.080317725,
HFdefUL(51,0) = -0.102431993
HFdefUL(1,1) = 9969.897594,40852.26331,40421.8854,39969.95537,39495.54763,38997.75107,38475.67622,37928.46325
37355.29119,36755.38829,
HFdefUL(11,1) = 36128.04364,35472.62011,34788.56878,34075.44487,33332.92516,32560.82708,31759.12936,30927.99429
30067.79142,29179.12276,
HFdefUL(21,1) = 28262.84904,27320.117,26352.38721,25361.462,24349.51291,7956.169122,40852.26331,40421.8854
39969.95537,39495.54763,
HFdefUL(31,1) = 38997.75107,38475.67622,37928.46325,37355.29119,36755.38829,36128.04364,35472.62011,34788.56878
34075.44487,33332.92516,
HFdefUL(41,1) = 32560.82708,31759.12936,30927.99429,30067.79142,29179.12276,28262.84904,27320.117,26352.38721
25361.462,24349.51291,
HFdefUL(51,1) = 5942.440651
HFdefUL(51,1) = 9390.379002
CMSEL,s,HF
SF,all,HFLUX,%HFdefUL%
alls
```

Figure C.1: Heat flux distribution on a SAS iris.

# D. FLUID-THERMAL (APDL) COMMAND SNIPPET

```
ET,matid,FLUID116
KEYOPT,matid,1,1 ! Temperature DOF only
KEYOPT,matid,2,1 ! Pass the information to Surface Elements
! Define Real Constants
MY_HD = 0.006
MY_CROSSSECTION = 3.14159*MY_HD*MY_HD/4
! Real Constant set
R,matid, MY_HD,MY_CROSSSECTION,1

finish
/PREP7

**********************************************************************************
!Cooling
et, 5000, 152        ! Type number 500 is arbitrary, surface element type
keyopt, 5000, 4, 0 ! Has mind side nodes that match adjacent elements
keyopt, 5000, 5, 1 ! Use extra node
keyopt, 5000, 6, 0 ! Extra node temperature is the bulk temperature
keyopt, 5000, 8, 2 ! Evaluate temperature dependent HTC at average film temperature
keyopt, 5000, 9, 0 ! Do not include radiation
Type, 5000

! convectionsurf is named component of nodes on convection surfaces
! Conv and FLUID are the named component of fluid elements
! NDSURF - Generates surface elements and connects them to the fluids

ndsurf,’Conv’,’FLUID’,3 ! Hole pipeline

! Specification of mass flows
```

```
cmsel,s,FLUID
sfe,all,,hflux,,19.05916e-3 ! Mass flow in the pipe
esel,s,type,,5000
sfe, all,, conv,,5079 ! Heat transfer coefficient udes with all surface elements

alls
fini
/solu
finish
/PREP7
```

# E. ANSYS BUSHING JOINT DEFINITION MATRICES

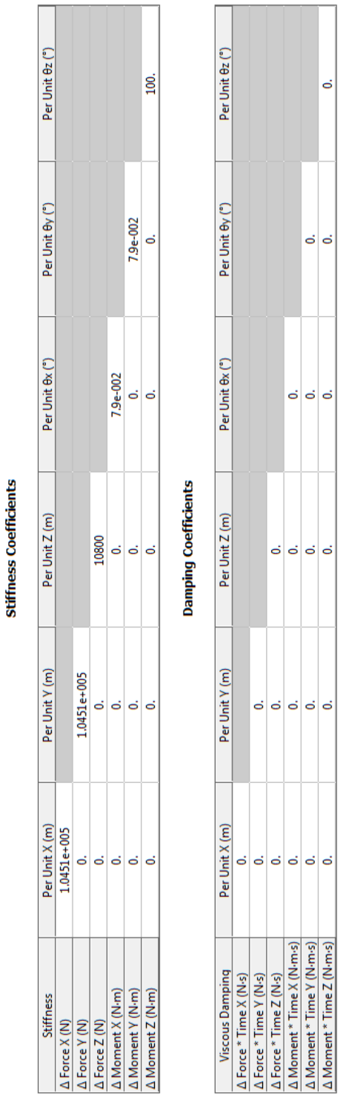

**Stiffness Coefficients**

| Stiffness | Per Unit X (m) | Per Unit Y (m) | Per Unit Z (m) | Per Unit θx (°) | Per Unit θy (°) | Per Unit θz (°) |
|---|---|---|---|---|---|---|
| Δ Force X (N) | 1.0451e+005 | | | | | |
| Δ Force Y (N) | 0. | 1.0451e+005 | | | | |
| Δ Force Z (N) | 0. | 0. | 10800 | | | |
| Δ Moment X (N·m) | 0. | 0. | 0. | 7.9e-002 | | |
| Δ Moment Y (N·m) | 0. | 0. | 0. | 0. | 7.9e-002 | |
| Δ Moment Z (N·m) | 0. | 0. | 0. | 0. | 0. | 100. |

**Damping Coefficients**

| Viscous Damping | Per Unit X (m) | Per Unit Y (m) | Per Unit Z (m) | Per Unit θx (°) | Per Unit θy (°) | Per Unit θz (°) |
|---|---|---|---|---|---|---|
| Δ Force * Time X (N·s) | 0. | | | | | |
| Δ Force * Time Y (N·s) | 0. | 0. | | | | |
| Δ Force * Time Z (N·s) | 0. | 0. | 0. | | | |
| Δ Moment * Time X (N·m·s) | 0. | 0. | 0. | 0. | | |
| Δ Moment * Time Y (N·m·s) | 0. | 0. | 0. | 0. | 0. | |
| Δ Moment * Time Z (N·m·s) | 0. | 0. | 0. | 0. | 0. | 0. |

Figure E.1: Bellows axial, lateral and rotational stiffness values for the DB interconnections.

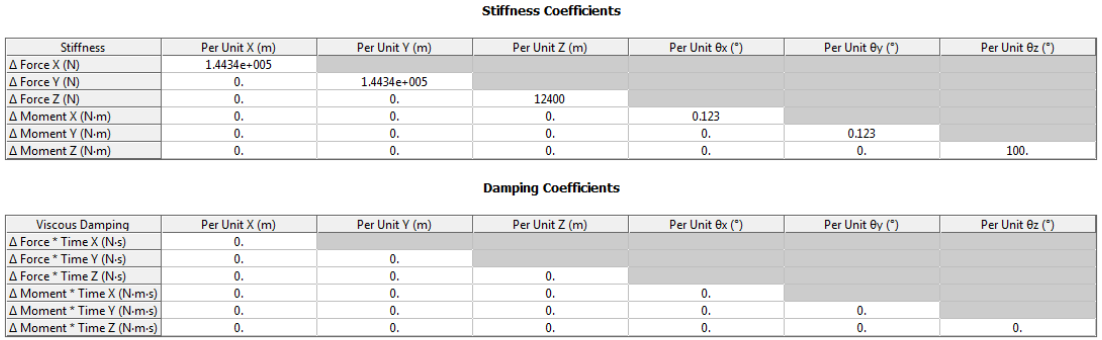

**Stiffness Coefficients**

| Stiffness | Per Unit X (m) | Per Unit Y (m) | Per Unit Z (m) | Per Unit θx (°) | Per Unit θy (°) | Per Unit θz (°) |
|---|---|---|---|---|---|---|
| Δ Force X (N) | 1.4434e+005 | | | | | |
| Δ Force Y (N) | 0. | 1.4434e+005 | | | | |
| Δ Force Z (N) | 0. | 0. | 12400 | | | |
| Δ Moment X (N·m) | 0. | 0. | 0. | 0.123 | | |
| Δ Moment Y (N·m) | 0. | 0. | 0. | 0. | 0.123 | |
| Δ Moment Z (N·m) | 0. | 0. | 0. | 0. | 0. | 100. |

**Damping Coefficients**

| Viscous Damping | Per Unit X (m) | Per Unit Y (m) | Per Unit Z (m) | Per Unit θx (°) | Per Unit θy (°) | Per Unit θz (°) |
|---|---|---|---|---|---|---|
| Δ Force * Time X (N·s) | 0. | | | | | |
| Δ Force * Time Y (N·s) | 0. | 0. | | | | |
| Δ Force * Time Z (N·s) | 0. | 0. | 0. | | | |
| Δ Moment * Time X (N·m·s) | 0. | 0. | 0. | 0. | | |
| Δ Moment * Time Y (N·m·s) | 0. | 0. | 0. | 0. | 0. | |
| Δ Moment * Time Z (N·m·s) | 0. | 0. | 0. | 0. | 0. | 0. |

Figure E.2: Bellows axial, lateral and rotational stiffness values for the RF network interconnections.

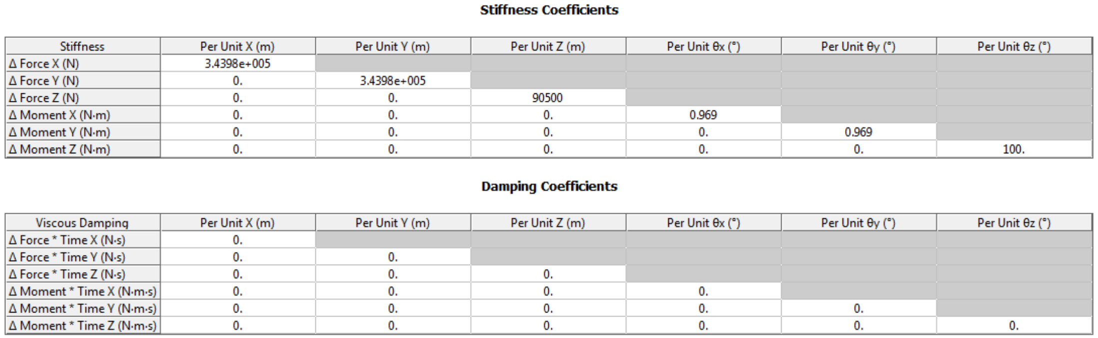

**Stiffness Coefficients**

| Stiffness | Per Unit X (m) | Per Unit Y (m) | Per Unit Z (m) | Per Unit θx (°) | Per Unit θy (°) | Per Unit θz (°) |
|---|---|---|---|---|---|---|
| Δ Force X (N) | 3.4398e+005 | | | | | |
| Δ Force Y (N) | 0. | 3.4398e+005 | | | | |
| Δ Force Z (N) | 0. | 0. | 90500 | | | |
| Δ Moment X (N·m) | 0. | 0. | 0. | 0.969 | | |
| Δ Moment Y (N·m) | 0. | 0. | 0. | 0. | 0.969 | |
| Δ Moment Z (N·m) | 0. | 0. | 0. | 0. | 0. | 100. |

**Damping Coefficients**

| Viscous Damping | Per Unit X (m) | Per Unit Y (m) | Per Unit Z (m) | Per Unit θx (°) | Per Unit θy (°) | Per Unit θz (°) |
|---|---|---|---|---|---|---|
| Δ Force * Time X (N·s) | 0. | | | | | |
| Δ Force * Time Y (N·s) | 0. | 0. | | | | |
| Δ Force * Time Z (N·s) | 0. | 0. | 0. | | | |
| Δ Moment * Time X (N·m·s) | 0. | 0. | 0. | 0. | | |
| Δ Moment * Time Y (N·m·s) | 0. | 0. | 0. | 0. | 0. | |
| Δ Moment * Time Z (N·m·s) | 0. | 0. | 0. | 0. | 0. | 0. |

Figure E.3: Bellows axial, lateral and rotational stiffness values for the Vacuum tank interconnections.

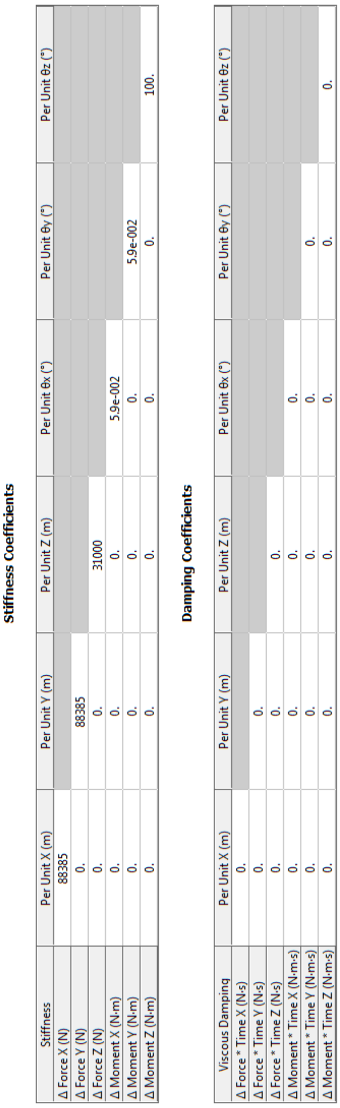

**Stiffness Coefficients**

| Stiffness | Per Unit X (m) | Per Unit Y (m) | Per Unit Z (m) | Per Unit θx (°) | Per Unit θy (°) | Per Unit θz (°) |
|---|---|---|---|---|---|---|
| Δ Force X (N) | 88385 | | | | | |
| Δ Force Y (N) | 0. | 88385 | | | | |
| Δ Force Z (N) | 0. | 0. | 31000 | | | |
| Δ Moment X (N·m) | 0. | 0. | 0. | 5.9e-002 | | |
| Δ Moment Y (N·m) | 0. | 0. | 0. | 0. | 5.9e-002 | |
| Δ Moment Z (N·m) | 0. | 0. | 0. | 0. | 0. | 100. |

**Damping Coefficients**

| Viscous Damping | Per Unit X (m) | Per Unit Y (m) | Per Unit Z (m) | Per Unit θx (°) | Per Unit θy (°) | Per Unit θz (°) |
|---|---|---|---|---|---|---|
| Δ Force * Time X (N·s) | 0. | | | | | |
| Δ Force * Time Y (N·s) | 0. | 0. | | | | |
| Δ Force * Time Z (N·s) | 0. | 0. | 0. | | | |
| Δ Moment * Time X (N·m·s) | 0. | 0. | 0. | 0. | | |
| Δ Moment * Time Y (N·m·s) | 0. | 0. | 0. | 0. | 0. | |
| Δ Moment * Time Z (N·m·s) | 0. | 0. | 0. | 0. | 0. | 0. |

Figure E.4: Bellows axial, lateral and rotational stiffness values for the Spider network interconnections.

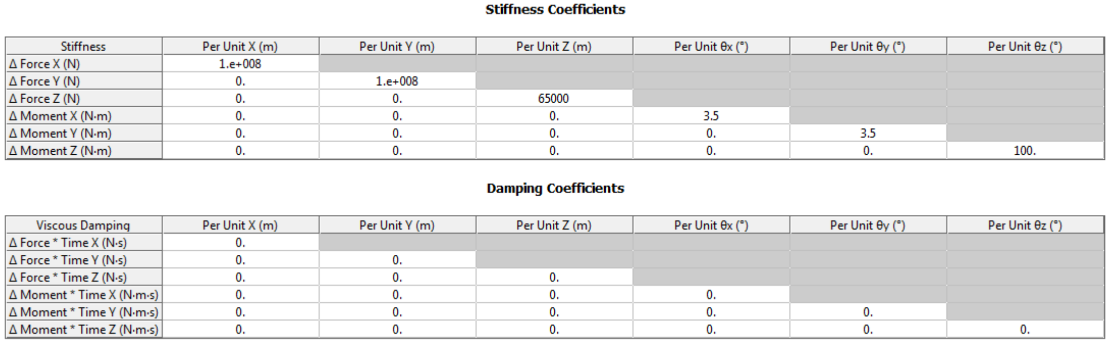

**Stiffness Coefficients**

| Stiffness | Per Unit X (m) | Per Unit Y (m) | Per Unit Z (m) | Per Unit θx (°) | Per Unit θy (°) | Per Unit θz (°) |
|---|---|---|---|---|---|---|
| Δ Force X (N) | 1.e+008 | | | | | |
| Δ Force Y (N) | 0. | 1.e+008 | | | | |
| Δ Force Z (N) | 0. | 0. | 65000 | | | |
| Δ Moment X (N·m) | 0. | 0. | 0. | 3.5 | | |
| Δ Moment Y (N·m) | 0. | 0. | 0. | 0. | 3.5 | |
| Δ Moment Z (N·m) | 0. | 0. | 0. | 0. | 0. | 100. |

**Damping Coefficients**

| Viscous Damping | Per Unit X (m) | Per Unit Y (m) | Per Unit Z (m) | Per Unit θx (°) | Per Unit θy (°) | Per Unit θz (°) |
|---|---|---|---|---|---|---|
| Δ Force * Time X (N·s) | 0. | | | | | |
| Δ Force * Time Y (N·s) | 0. | 0. | | | | |
| Δ Force * Time Z (N·s) | 0. | 0. | 0. | | | |
| Δ Moment * Time X (N·m·s) | 0. | 0. | 0. | 0. | | |
| Δ Moment * Time Y (N·m·s) | 0. | 0. | 0. | 0. | 0. | |
| Δ Moment * Time Z (N·m·s) | 0. | 0. | 0. | 0. | 0. | 0. |

Figure E.5: Bellows axial, lateral and rotational stiffness values for the SAS interconnections.

# F. TEMPERATURE CONTOURS FOR THE SAS UNDER RF LOAD

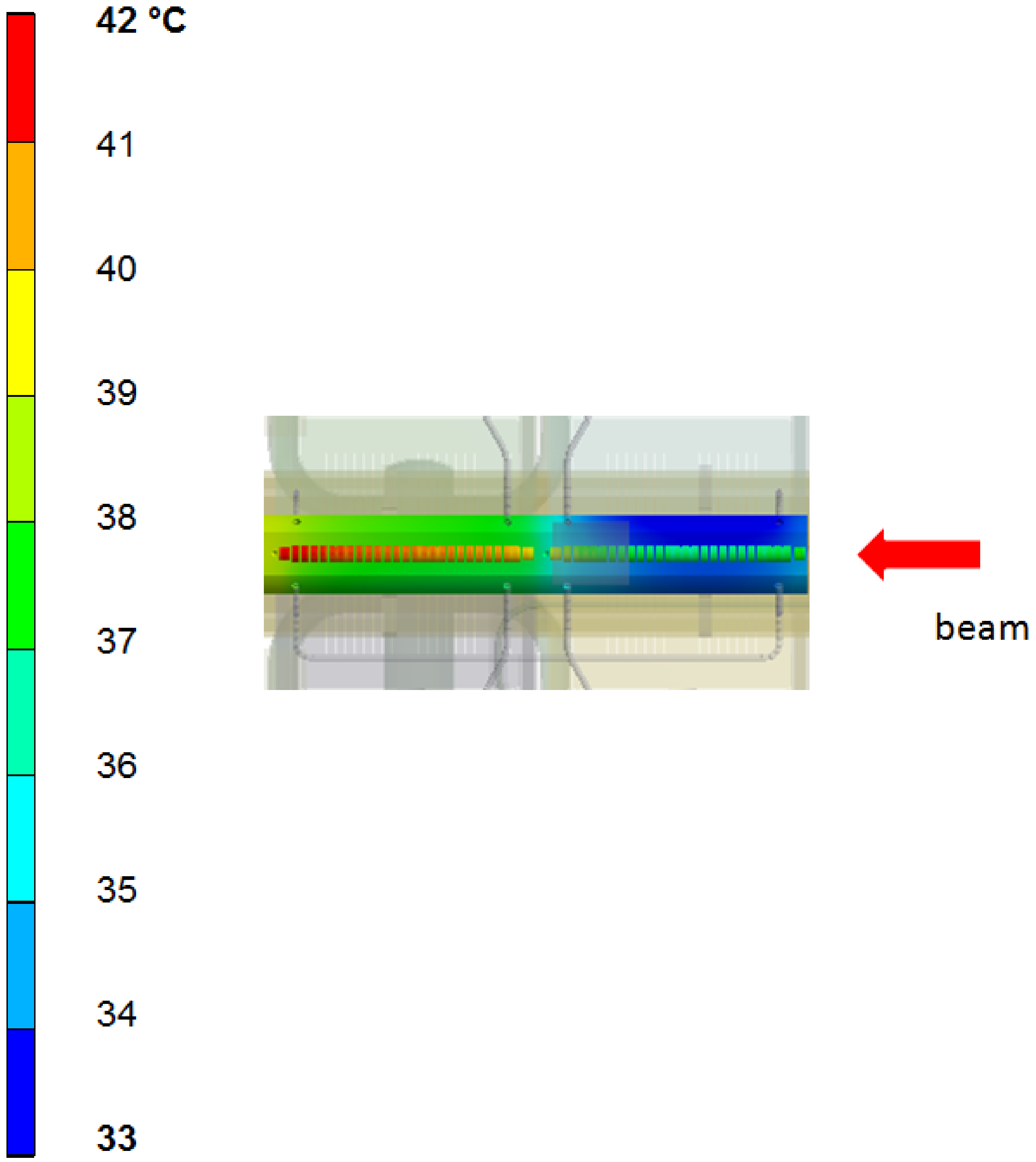

Figure F.1: Temperature contours for the SAS under RF load.

# G. DEFORMATION CONTOURS FOR THE MODULE UNDER GRAVITY LOAD

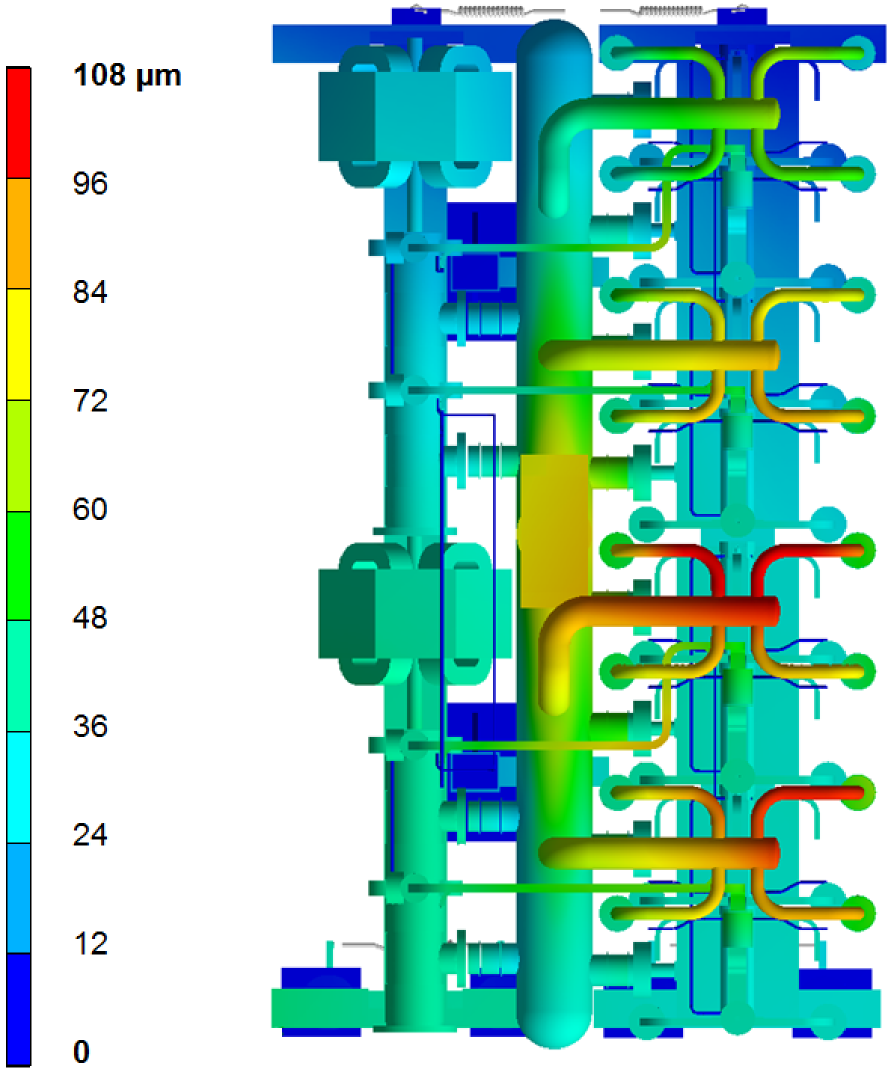

Figure G.1: Deformation contours for the module under gravity load.

# H. DEFORMATION CONTOURS FOR THE SAS UNDER RF LOAD

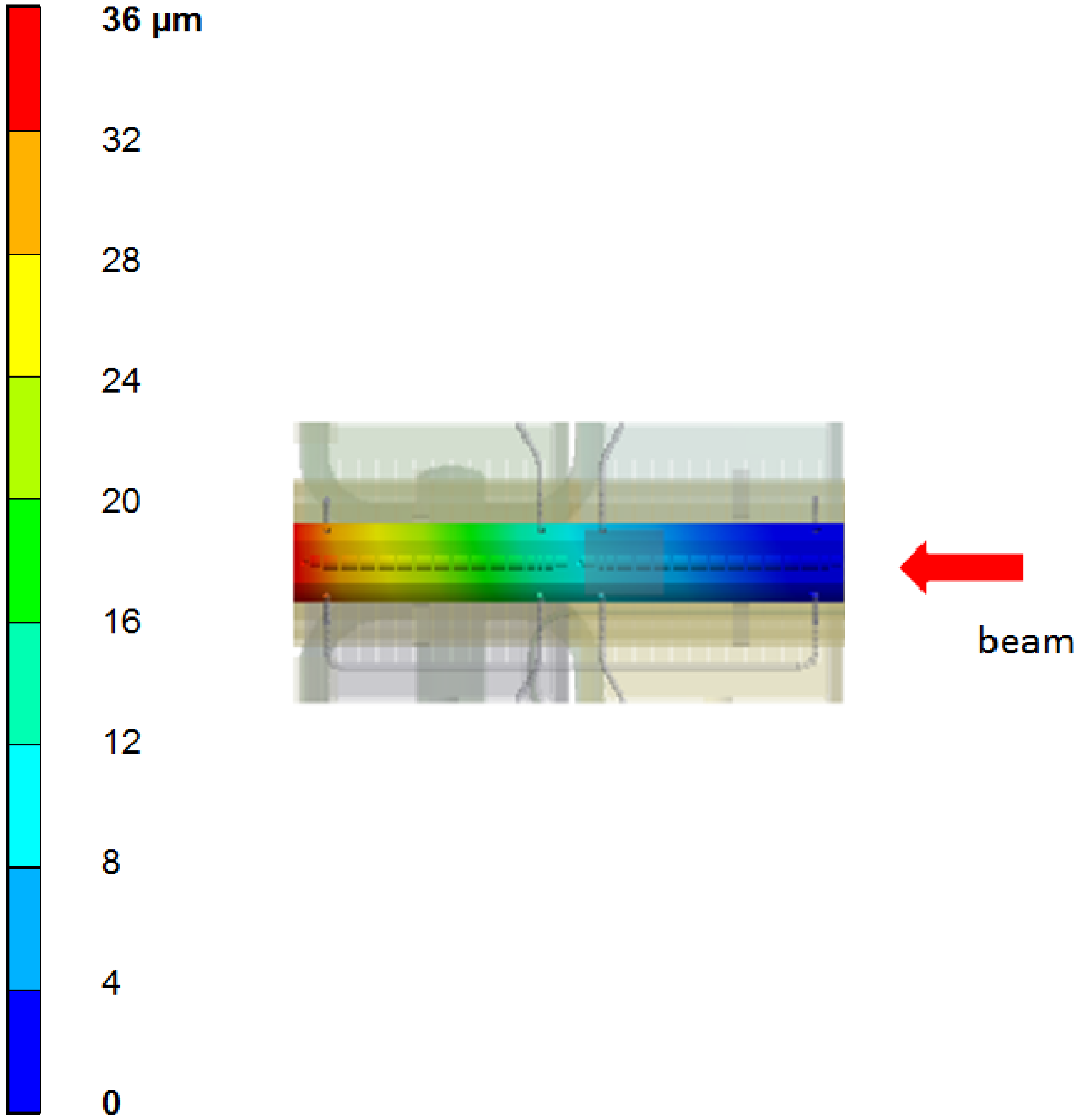

Figure H.1: Deformation contours for the SAS under RF load.